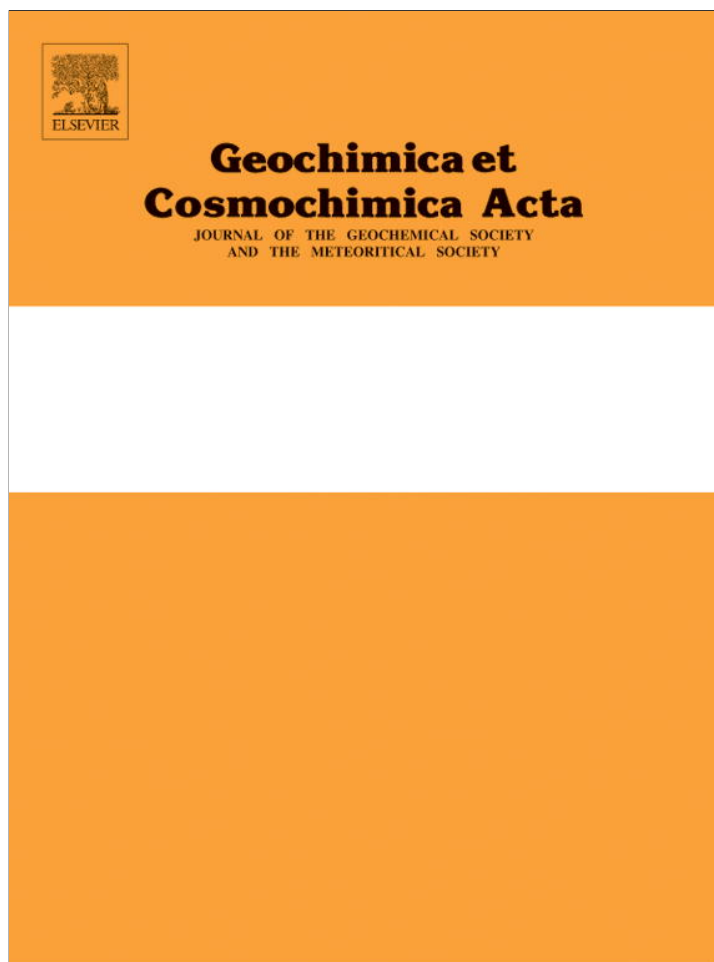


Provided for non-commercial research and education use.  
Not for reproduction, distribution or commercial use.



(This is a sample cover image for this issue. The actual cover is not yet available at this time.)

**This article appeared in a journal published by Elsevier. The attached copy is furnished to the author for internal non-commercial research and education use, including for instruction at the authors institution and sharing with colleagues.**

**Other uses, including reproduction and distribution, or selling or licensing copies, or posting to personal, institutional or third party websites are prohibited.**

**In most cases authors are permitted to post their version of the article (e.g. in Word or Tex form) to their personal website or institutional repository. Authors requiring further information regarding Elsevier's archiving and manuscript policies are encouraged to visit:**

**<http://www.elsevier.com/copyright>**



# Integrated multi-site U–Th chronology of the last glacial Lake Lisan

Adi Torfstein<sup>a,\*</sup>, Steven L. Goldstein<sup>a,b</sup>, Elisa J. Kagan<sup>c,d,1</sup>, Mordechai Stein<sup>c</sup>

<sup>a</sup> Lamont–Doherty Earth Observatory of Columbia University, 61 Rt. 9W, Palisades, NY 10964, USA

<sup>b</sup> Department of Earth and Environmental Sciences, Columbia University, 61 Rt. 9W, Palisades, NY 10964, USA

<sup>c</sup> Geological Survey of Israel, 30 Malkhe Israel Street, Jerusalem 95501, Israel

<sup>d</sup> Institute of Earth Sciences, The Hebrew University of Jerusalem, Jerusalem 91904, Israel

Received 23 February 2012; accepted in revised form 2 November 2012; Available online 29 November 2012

## Abstract

We present a new integrated multi-site chronology for Lake Lisan, which occupied the Dead Sea basin and Jordan Valley during the last glacial period (70–14 kka, Marine Isotope Stages 4, 3, 2). The Dead Sea basin lacustrine deposits are unique among closed basin sediments in that they formed in a deep, hypersaline water body that precipitated primary aragonite which is amenable to radiometric dating by U-series, providing a solid basis for studies of the relationship of Middle East climate to other changes in the high latitudes or the tropics.

The application of U–Th dating for lacustrine carbonates requires corrections for detrital U and Th and hydrogenous (“initial”) <sup>230</sup>Th. Here we followed an iterative approach, in which we evaluate the composition of the detrital contamination independently for every set of coeval samples to determine the corrected ages. These were further filtered and combined with lithological–limnological considerations, which were used to construct age–height models for all studied stratigraphic sections. Finally, the ages of stratigraphic tie-points were used to integrate the individual age–height models into a unified chronology. The resulting chronological framework indicates that the ages of several primary gypsum units associated with catastrophic lake level drops correspond with the timing of Heinrich events in the North Atlantic. Thus, a final iterative step involves refining the ages of “Lisan-gypsum events” based on the ages of Heinrich events 6, 5, 5a, 4, and 1. This approach yields an unprecedented basin-wide, unified, event-anchored chronology for the Lisan Formation, with typical age uncertainties ca. 1000–2000 years (95% confidence limit) across the entire last glacial, well below those typically related to individual U–Th and radiocarbon dating of “dirty” carbonates from similar time intervals. The results can be further extrapolated to new sites and serve as a geochronometric reference for the reconstruction of the limnological history of Lake Lisan.

© 2012 Elsevier Ltd. All rights reserved.

## 1. INTRODUCTION

Accurate and high-resolution calendar chronologies are critical for reconstructing the paleo-hydrological and paleo-environmental histories of continental regions and allow comparison with regional and global climate archives such

as ice cores and deep-sea cores. Common terrestrial archives that are used include speleothems, travertines and lacustrine carbonates. Speleothems provide accurate ages up to the U–Th dating limit of several hundreds of kyrs, but their appearance is limited to specific environments (e.g., Wang et al., 2001, 2008; Bar-Matthews et al., 2003; Richards and Dorale, 2003; Partin et al., 2007). Dating of travertine and lake carbonate deposits is more challenging because the primary minerals are often contaminated by detrital material and contain initial hydrogenous thorium, requiring correction procedures (e.g., Kaufman, 1971, 1993; Ludwig and Titterton, 1994; Lin et al., 1996;

\* Corresponding author.

E-mail address: [adi.torf@ldeo.columbia.edu](mailto:adi.torf@ldeo.columbia.edu) (A. Torfstein).

<sup>1</sup> Current address: The Department of Geophysics and Planetary Sciences, Tel Aviv University, Tel Aviv 69978, Israel.

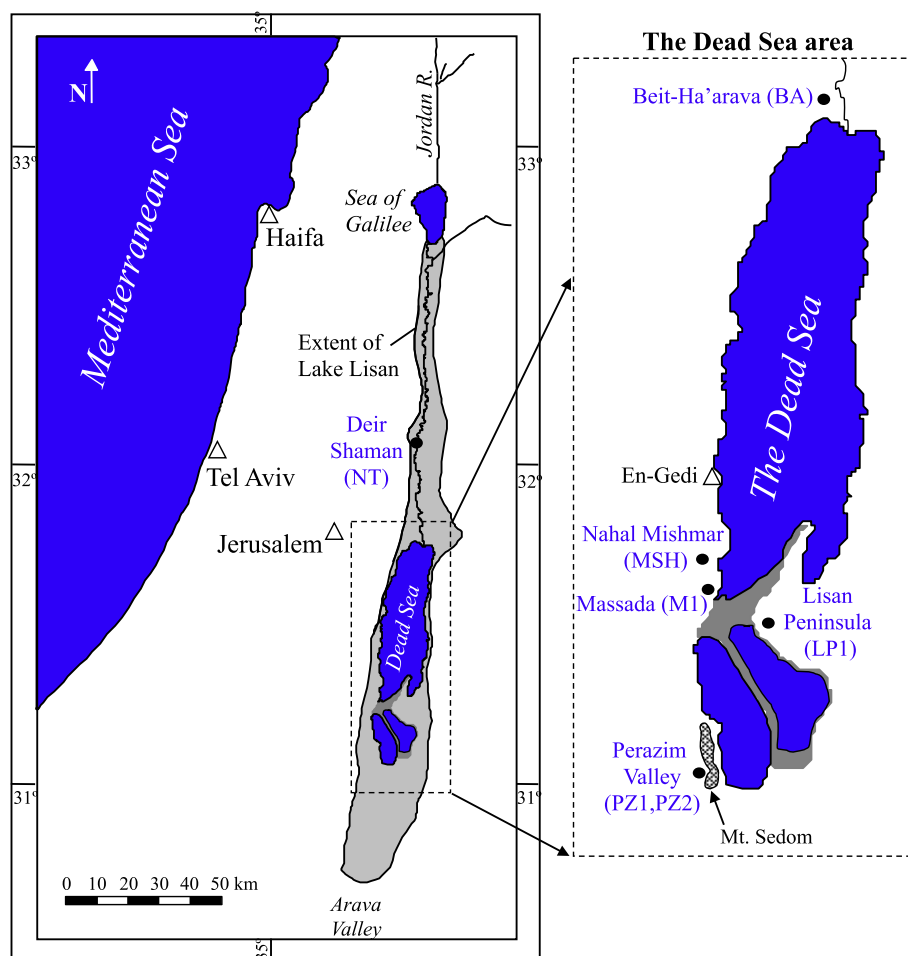


Fig. 1. Location map. The main sections, locations, and base elevations discussed here are: Perazim Valley *PZ1*, 31°05'41N, 35°21'31E, 306 m-bmsl; Massada *M1*, 31°18'33N, 35°22'34E, 374 m-bmsl; Nahal Mishmar *MSH*, 31°21'58N, 35°22'38E, 375 m-bmsl; Beit-Ha'arava *BA*, 31°47'43N, 35°30'28E, 365 m-bmsl; Deir-Shaman *NT*, 32°03'15N, 35°31'24E, 369 m-bmsl; and Lisan Peninsula *LP1*, 31°15'17N, 35°25'36E, ~380 m-bmsl. Elevation data from Waldmann et al. (2009).

Israelson et al., 1997; Ku et al., 1998; Schramm et al., 2000; Ludwig, 2003; Haase-Schramm et al., 2004).

The Lisan Formation, comprising sediments deposited in the last glacial cycle of the Dead Sea termed Lake Lisan, has been shown to be a sensitive recorder of the hydrology and climate of the watershed of the Dead Sea Basin (*DSB*) and the Levant (Neev and Emery, 1967; Begin et al., 1974; Katz et al., 1977; Stein et al., 1997; Stein, 2001; Bartov et al., 2003; and references therein). In an attempt to establish a high-resolution and accurate chronology of Lake Lisan, Haase-Schramm et al. (2004) investigated approaches for correcting the contributions of detrital U and Th and hydrogenous Th in the primary aragonite, and compared the corrected U–Th ages to atmospheric  $^{14}\text{C}$  ages, producing an age–height regression for a single stratigraphic section of the Lisan Formation (the *PZ1* section located in the Perazim Valley; Fig. 1).

Here, we establish an integrated multi-site chronology for Lake Lisan that combines age–height models based on U–Th dating, previously determined  $^{14}\text{C}$  ages, and field observations. New age–height models are presented for five

different stratigraphic sections of the Lisan Formation along the DSB: Massada (*M1*), Nahal Mishmar (*MSH*), Beit-Ha'arava (*BA*), Deir-Shaman (*NT*), and the Lisan Peninsula (*LP1*). The new age–height models are combined with the *PZ1* chronology (Haase-Schramm et al., 2004) and used to determine ages of prominent events of gypsum deposition associated with abrupt lake drops. These in turn are compared to other well-dated archives and applied as age anchor points for constructing a unified chronology of Lake Lisan's history.

## 2. BACKGROUND

### 2.1. Limnological characteristics

Several water bodies occupied the tectonic depressions along the Dead Sea Rift valley during the Neogene–Quaternary (Fig. 1). The size and composition of these water bodies – the late Neogene Sedom Lagoon, the Pleistocene Lake Amora, the last glacial Lake Lisan and the Holocene

Dead Sea – changed with time (Stein, 2001). The ongoing supply of freshwater into the hypersaline water bodies had substantial impact on their physical and chemical properties, whereby water column stratification was induced by density differences, and the chemical composition of the water reflected the interplay of freshwater and Ca-chloride brine inputs, each with differing ion compositions. During high lake stands and positive freshwater input, the lakes had a two-layer structure (a less saline surface layer overlying a hypersaline brine), and deposited annual sequences of primary aragonite, which precipitated from the shallow layer, and silty to clay-sized detritus, which are mainly quartz and calcite grains of eolian origin (termed “alternating aragonite–detritus”, or “*aad facies*”; Marco, 1996). Thus, intervals of deposition of primary aragonite imply significant supply of freshwater to the lake, and a stable less saline surface layer, which in turn indicates enhanced precipitation in the DSB drainage area. During more arid phases, the lakes deposited less aragonite and more detritus, along with occasional layers of gypsum when the two-layer density structure became unstable, and the lake overturned. Hence, shifts in water column composition and configuration reflect the climatic–hydrologic conditions of the region, which varied during the Quaternary from arid to semi-arid conditions (Neev and Emery, 1967; Begin et al., 1974; Katz et al., 1977; Stein et al., 1997; Stein, 2001; Bartov et al., 2003; Bookman (Ken-Tor) et al., 2004; Torfstein et al., 2005, 2008, 2009; Bookman et al., 2006; Migowski et al., 2006; and references therein).

Throughout the last glacial, Lake Lisan maintained significantly higher water levels (~160–330 m below mean sea level, henceforth *m-bmsl*; Bartov et al., 2003) compared to the last interglacial water-body (Lake Amora, which had an estimated average water elevation of ~350 m-bmsl; Waldmann et al., 2007, 2009), and the Holocene Dead Sea (whose average elevation is ~400 m-bmsl; Yechieli et al., 1993; Bookman (Ken-Tor) et al., 2004; Migowski et al., 2006).

## 2.2. Stratigraphy of the Lisan Formation

Machlus et al. (2000) divided the Lisan Formation into three stratigraphic units (Figs. 2, 3, and EA1) based on the lithology and stratigraphy of the PZ1 section at Perazim Valley. The Lower and Upper Members are composed mainly of the *aad facies*, while the Middle Member is characterized by many clastic (sand and silt) layers, and laminated gypsum, as well as *aad* sequences. The Lower and Upper members are capped by the Lower and Upper Gypsum Units (LGU and UGU), respectively (Torfstein et al., 2005, 2008).

The *aad* sequences that characterize the Lower and Upper Members were deposited during high lake-level conditions, corresponding to the colder Marine Isotope Stage (MIS) 4 and 2 intervals, respectively. The increased abundance of clastic material such as sands, pebbles and thick sequences of silty detritus in the Middle Member reflects frequent low lake-stand conditions that prevailed during the warmer MIS 3 (Stein, 2001; Bartov et al., 2003; Haase-Schramm et al., 2004).

At Massada (M1) the base of the Lisan Formation is located at 374 m-bmsl, some 70 m lower (deeper in the paleo-lake) than the base of PZ1 at 306 m-bmsl (Waldmann et al., 2007). The M1, MSH, LP1 and BA sections have fewer clastic layers than PZ1, and are dominated by primary precipitate (e.g., aragonite, gypsum). The Deir-Shaman (NT) site is the northern-most site studied here, located closest to the sources of freshwater. Its base elevation is slightly higher than M1 at 369 m-bmsl (Waldmann et al., 2009), and the Lower and Upper Members at NT reflect a deep water depositional environment, similar to synchronous layers at the M1 and PZ1 sites; namely, they are mainly comprised of *aad* sequences and are capped by the LGU and UGU, respectively. The Middle Member at Deir-Shaman contains thick bundles of detritus with three short occurrences of *aad* intervals (henceforth referred to as the Middle Member Aragonite Units; MMAU).

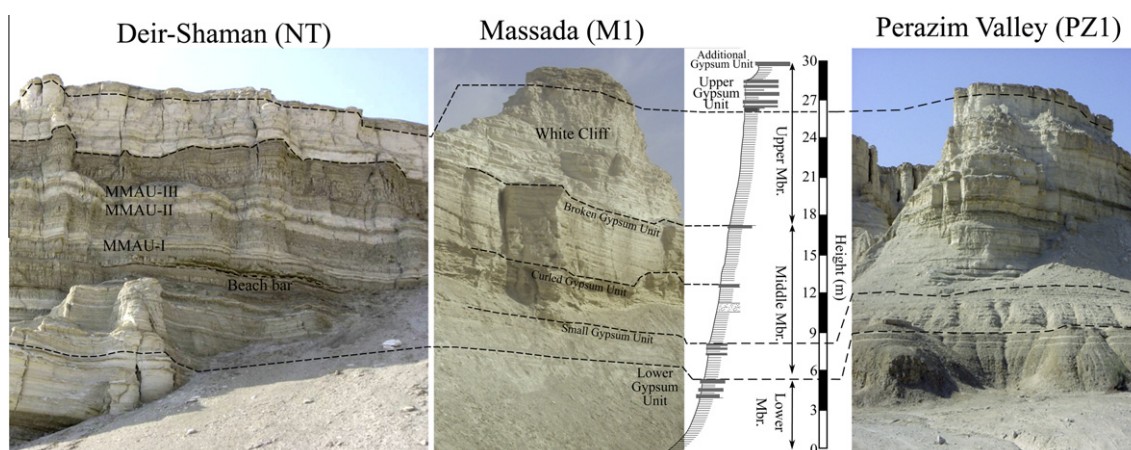


Fig. 2. Sections at Perazim Valley (PZ1), Massada (M1) and Deir-Shaman (NT). The columnar section refers to the M1 section, “Height” pertains (here and throughout the paper) to the height above the base of the Lisan Formation at each location. The deep-water depositional environment at M1 is reflected by high content of white aragonite laminae and massive gypsum layers throughout the section, while the marginal NT and PZ1 sites are characterized by a higher abundance of clastics, particularly in the Middle Member. The three Middle Member Aragonite Units (MMAU) at Deir-Shaman reflect lake level highs during MIS3.

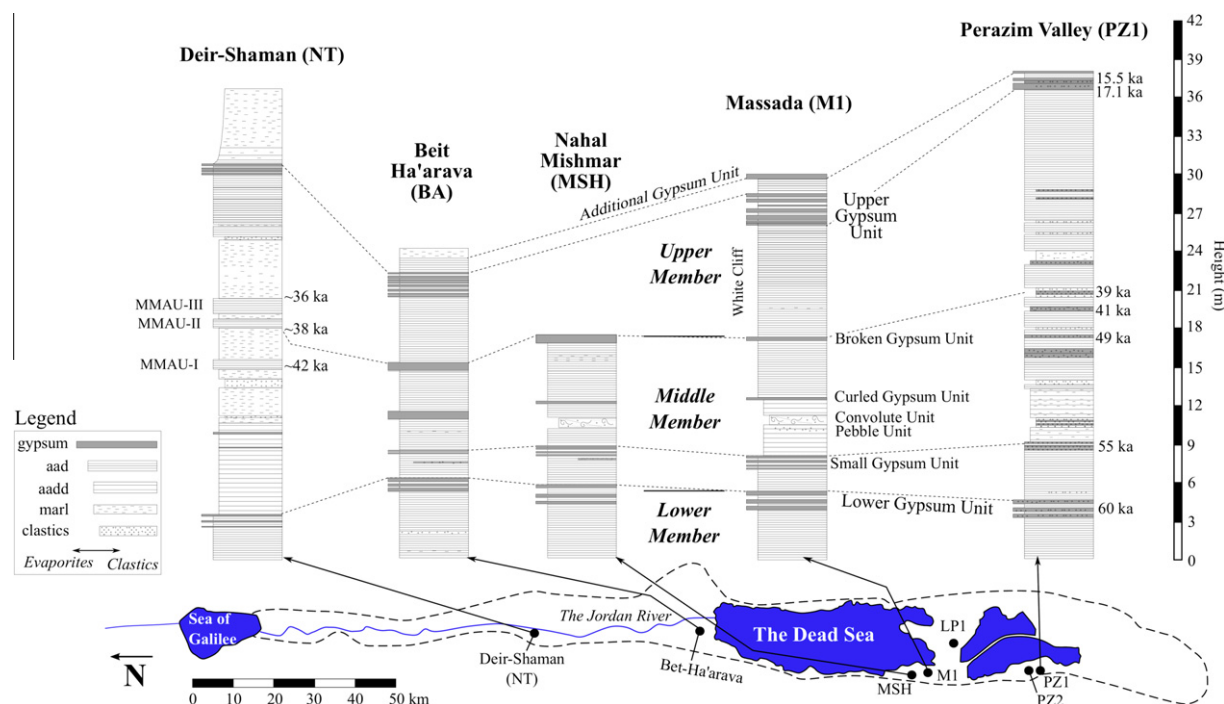


Fig. 3. Lisan stratigraphy at Perazim Valley (PZ1), Massada (M1), Nahal Mishmar (MSH), Beit-Ha'arava (BA) and Deir-Shaman (NT). (A) The sections are shown in geographic order from north (NT) to south (PZ1). The LP1 section is similar to M1 and is not presented. The two marginal sites of PZ1 and NT are thicker than M1, reflecting influx of clastic material to the marginal sites that results in short-term higher sedimentation rates. Legend abbreviations: *aad* – alternating aragonite–detritus laminae, *aadd* – detritus-dominated *aad*. M1 contains a “mixed” convolute unit at ~11 m T (details are given in Bartov et al. (2002)) and is likely associated with a similar layer at MSH.

### 2.3. Stratigraphic anchor-points

Several prominent stratigraphic markers, typically gypsum layers associated with lake level drops, can be traced over large areas within the Dead Sea basin (Figs. 1–3):

- (1) Three prominent gypsum layers comprising the *Lower Gypsum Unit (LGU)* cap the Lower Member of the Lisan Formation.
- (2) The *Small Gypsum Unit* at M1 occurs as three layers of sand and gypsum at PZ1, located ~3.5 m above the LGU. The cumulative thickness of gypsum in this unit increases at M1 and BA.
- (3) A gypsum layer termed the *Curled Gypsum Unit* at M1 (Torfstein et al., 2008) is present at LP1, MSH, and BA. This unit is not identified at PZ1 and NT, where it correlates to sedimentary unconformities.
- (4) The *Broken Gypsum Unit* appears at M1, LP1, MSH, and BA.
- (5) All sections discussed here, with the exception of MSH, contain an *Upper Gypsum Unit (UGU)*, which caps a thick interval of *aad* deposited during MIS 2 known as the “White Cliff”.
- (6) At M1, the *Additional Gypsum Unit* appears about 1.16 m above the UGU and can be correlated to remnants at the top of PZ1, and a silt layer at BA. This unit represents the youngest sediment sequence

known from Lake Lisan, after which the lake level declined and remained at significantly lower stands throughout the Holocene.

### 3. OUTLINE

The integrated multi-site Lisan Formation chronology is established as follows. We first determine the individual ages at each individual section of the above-described gypsum layers through U–Th-based age–height models, combined with the previously constructed chronology of the PZ1 section (Haase-Schramm et al., 2004) and complementary radiocarbon and counting curve chronology of Massada (M1; Prasad et al., 2004). The individual age–height models at LP1, M1, BA, NT, PZ1 and MSH sections are shown in Fig. 9.

We subsequently calculate the weighted mean ages of each of the marker-gypsum layers described in Section 2.3. These show synchronicity, within the uncertainty, with Heinrich Events (*H-events*), episodes of massive iceberg discharge into the North Atlantic associated with abrupt cooling stadials in the Northern Hemisphere. Accordingly, we tie the ages of the marker-gypsum layers to those of *H-events* as determined in well-dated speleothem records, use the results to construct an integrated basin-wide chronology for the Lisan Formation, and establish Bayesian age–height models for each of the sections studied here.

## 4. METHODS

### 4.1. Field work and sample preparation

Samples approximately  $20 \times 20 \times 20 \text{ cm}^3$  in size were collected from several sections of the Lisan Formation along the DSB (Figs. 1–3). Approximately 5 g of aragonite, or detritus in *aad* layers, was separated from the bulk samples by scraping with a scalpel in a laminar flow-hood. Following grinding and homogenization, the mineralogical composition of selected samples was identified by X-ray diffraction in the Geological Survey of Israel (GSI).

### 4.2. U–Th dating

#### 4.2.1. Chemistry

Typically, 100 mg of homogenized aragonite powder were spiked with a mixed  $^{236}\text{U}$ – $^{229}\text{Th}$  spike and dissolved in 7 N  $\text{HNO}_3$ . Some additional samples, comprising of pure detritus or a mixture of aragonite and detritus, were similarly spiked and then digested using a  $\text{HNO}_3$ –HF mixture in order to achieve full dissolution of the silicate phase. Subsequently, all the dissolved samples were dried down and re-dissolved in 2 ml of 7 N  $\text{HNO}_3$ . The solutions were then loaded onto anion exchange columns filled with 2 ml of Bio-Rad AG 1X8 200–400 mesh resin. The resin was cleaned with 6 N HCl and 18.2 M $\Omega$  water, and preconditioned in two steps of 2 ml 7 N  $\text{HNO}_3$ . The samples were then loaded onto the columns after which Th was eluted using 6 N HCl and U was eluted using 1 N HBr. Both fractions were then dried and re-dissolved in 0.1 N  $\text{HNO}_3$ .

#### 4.2.2. Mass spectrometry

Measurements were performed using a multicollector inductively coupled plasma mass spectrometer (MC-ICP-MS) Nu Instruments Ltd. (UK) at the Geological Survey of Israel. The samples were introduced to the MC-ICP-MS through an Aridus<sup>®</sup> micro-concentric desolvating nebuliser sample introducing system. U and Th aliquots were measured separately. The U aliquot was measured in three cycles with alternate measurements of  $^{238}\text{U}$ ,  $^{236}\text{U}$ ,  $^{235}\text{U}$  and  $^{234}\text{U}$  on Faraday cups and ion counters in order to correct for their relative efficiencies and instrumental mass fractionation, which was corrected using the exponential mass fractionation law to the natural ratio of  $^{238}\text{U}/^{235}\text{U} = 137.88$ . Similarly, the Th aliquot was measured in three cycles of alternate analyses of  $^{232}\text{Th}$ ,  $^{230}\text{Th}$ ,  $^{229}\text{Th}$ ,  $^{238}\text{U}$  and  $^{235}\text{U}$  on Faraday cups and ion counters (Table 1). A standard reference material, NBL112a, was routinely introduced with the samples to check instrument performance. The  $^{234}\text{U}/^{238}\text{U}_{(\text{atomic})}$  ratio obtained for NBL 112a over the course of this study was  $527 \times 10^{-7} \pm 3$  ( $2\sigma$ ) in agreement with Cheng et al. (2000;  $528.6 \times 10^{-7} \pm 2.5$ ).

Decay constants per year used in this study are:  $\lambda_{230} = 9.1577 \times 10^{-6}$ ;  $\lambda_{232} = 4.9475 \times 10^{-11}$ ,  $\lambda_{234} = 2.8263 \times 10^{-6}$  and  $\lambda_{238} = 1.55125 \times 10^{-10}$  (Le Roux and Glendenin, 1963; Jaffey et al., 1971; Cheng et al., 2000). The high precision of  $^{238}\text{U}$  measurement on MC-ICP-MS allows for us to treat error correlations for the  $(^{232}\text{Th}/^{238}\text{U})$ – $(^{230}\text{Th}/^{238}\text{U})$  and  $(^{232}\text{Th}/^{238}\text{U})$ – $(^{234}\text{U}/^{238}\text{U})$

Table 1

Collector configuration for isotopic analysis of U and Th by MC-ICPMS.

Collector:	Ax	L1	L2	IC0	L3	IC1
<i>Uranium</i>						
Cycle 1	$^{238}\text{U}$			$^{235}\text{U}$		
Cycle 2			$^{238}\text{U}$			$^{235}\text{U}$
Cycle 3		$^{238}\text{U}$		$^{236}\text{U}$	$^{235}\text{U}$	$^{234}\text{U}$
Collector:	H4	H3	H1	Ax	L2	IC1
<i>Thorium</i>						
Cycle 1	$^{238}\text{U}$		$^{235}\text{U}$		$^{232}\text{Th}$	$^{229}\text{Th}$
Cycle 2					$^{238}\text{U}$	$^{235}\text{U}$
Cycle 3		$^{238}\text{U}$		$^{235}\text{U}$		$^{230}\text{Th}$

couplets as negligible. This is a conservative assumption because the existence of error correlations would dictate the true propagated age uncertainty to be smaller than reported (Ludwig and Titterton, 1994; Ludwig, 2003).

## 5. DATING LACUSTRINE SEQUENCES

### 5.1. U–Th dating of lacustrine carbonates

Under optimum circumstances,  $^{230}\text{Th}$ –U ages in carbonates showing U-series disequilibrium can be calculated by the following equation (after Broecker, 1963):

$$\left(\frac{^{230}\text{Th}}{^{238}\text{U}}\right) = (1 - e^{-\lambda_{230}t}) + \left(\left(\frac{^{234}\text{U}}{^{238}\text{U}}\right) - 1\right) \times \left(\frac{\lambda_{230}}{\lambda_{230} - \lambda_{234}}\right) \times (1 - e^{-(\lambda_{230} - \lambda_{234})t}), \quad (1)$$

where the isotope ratios presented are activity ratios. Eq. (1) assumes that samples have no initial  $^{230}\text{Th}$  and that all of the U is derived from the precipitating solution (in this case lake water). These assumptions are often valid for corals and speleothems, which typically contain negligible detrital Th and U, and negligible water-derived (hydrogenous) Th, but they rarely hold for other carbonates such as lake deposits or travertine. Primary lake carbonates are likely to contain U and Th from admixed detritus material, as well as hydrogenous Th. Many studies have tried to determine appropriate sample processing methods and corrections in order to obtain accurate U-series ages of “dirty” continental carbonates. They have discussed issues such as the advantages of whole rock dissolution vs. leaching, as well as different approaches for correcting detrital and hydrogenous contributions to the U and Th in individual samples and in coeval sample suites (e.g., Kaufman, 1971; Ku and Liang, 1984; Bischoff and Fitzpatrick, 1991; Luo and Ku, 1991; Kaufman, 1993; Haase-Schramm et al., 2004; Stein and Goldstein, 2006; and references therein).

Considering these issues, we used two complementary approaches to calculate  $^{230}\text{Th}$ –U ages of the carbonates:

- (1) *Single sample correction methods*, where the detrital U and Th and initial hydrogenous Th contributions are subtracted from individual sample measurements. The detrital U and Th correction values are

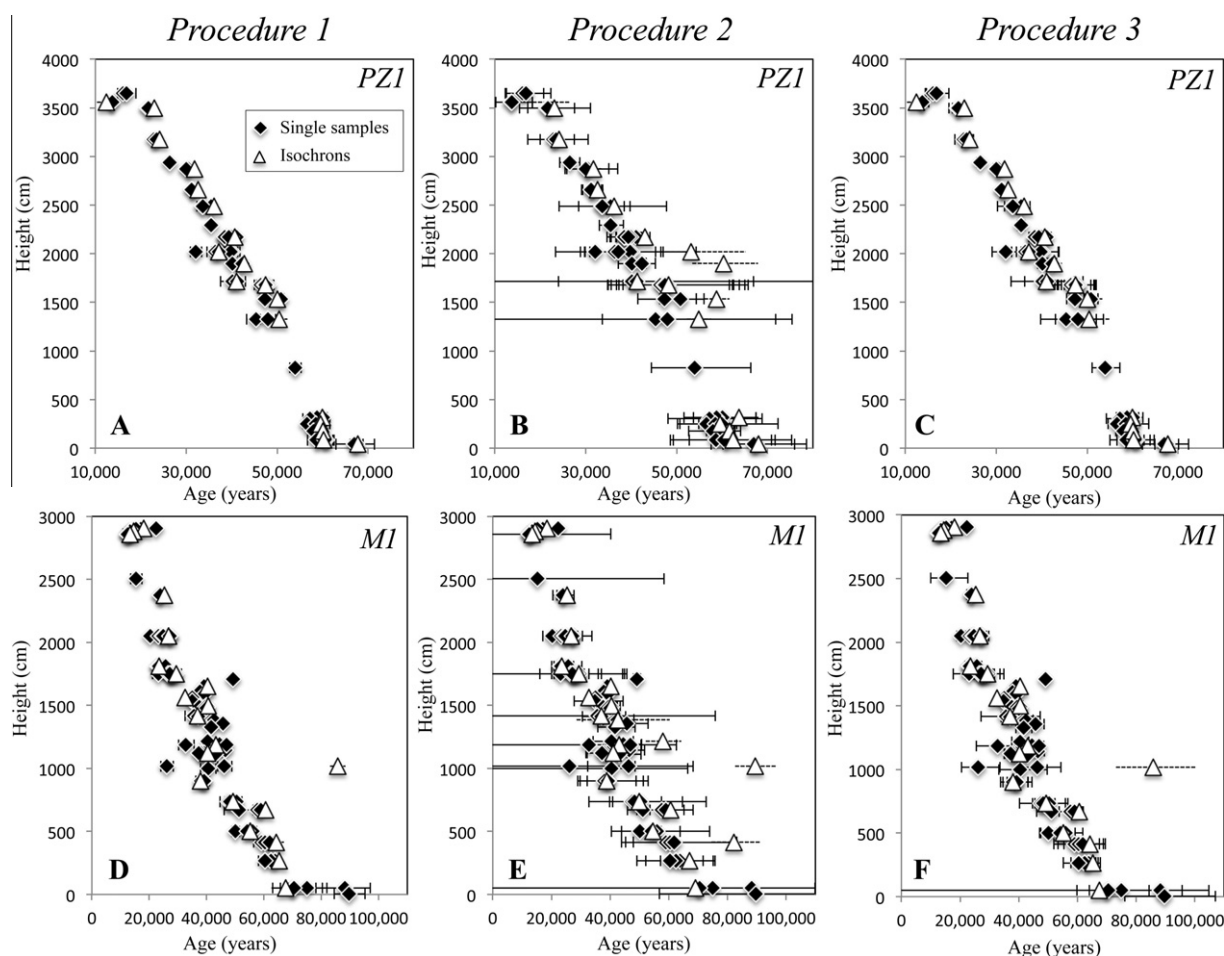


Fig. 4. Impact of different age calculation procedures on age–height models. Three age calculation procedures are tested for PZI (panels A–C) and MI (D–F): (1) a 10% detrital end-member (DEM) uncertainty (used by Haase-Schramm et al., 2004); (2) a 70% DEM uncertainty; (3) a 10% DEM uncertainty for isochron calculations and 30% for the single sample calculations. In procedures 2 and 3 (B, C, E, and F), the isochron uncertainties were further expanded by the square root of the MSWD, in order to account for observed scatter that exceeds the analytical scatter. Procedures 1 and 2 under- and over-estimate uncertainties, respectively, whereas procedure 3 provides a more realistic prediction of the scatter of the samples about a linear age–height curve.

determined either by direct measurement of “pure” detritus material or by extrapolation of isochron regression curves (further discussed below). The initial hydrogenous Th component might be determined empirically by using a sample of an independently known age (e.g., by  $^{14}\text{C}$  ages of organic material), where an apparent difference in the U–Th age could be attributed to the presence of initial  $^{230}\text{Th}$  after correcting for the detritus component. In this case, the extra initial  $^{230}\text{Th}$  is corrected by subtracting this component from the detritus-corrected values. Alternatively, the fraction of the hydrogenous Th can be retrieved from analyses of trace element chemistry of specific samples (for example, Th/Zr ratios, as discussed in Haase-Schramm et al., 2004). The presence of initial hydrogenous Th in a primary aragonite cannot be corrected using the isochron method.

- (2) *The isochron method*, which is often used to identify the U-series nuclide activities ( $^{230}\text{Th}/^{238}\text{U}$ ,  $^{234}\text{U}/^{238}\text{U}$ ) of the pure primary carbonate in sets of

coeval samples of “dirty” carbonates, in order that Eq. (1) can be used to determine the age. This assumes that a suite of samples formed at the same time, from mixtures of the same detrital component with primary Th-free carbonate. The ( $^{230}\text{Th}/^{238}\text{U}$ ) and ( $^{234}\text{U}/^{238}\text{U}$ ) ratios of detritus-free carbonate is retrieved from the y-intercepts of Osmond-type diagrams ( $^{232}\text{Th}/^{238}\text{U}$  vs.  $^{230}\text{Th}/^{238}\text{U}$ , and  $^{232}\text{Th}/^{238}\text{U}$  vs.  $^{234}\text{U}/^{238}\text{U}$ , respectively) or the slopes of Rosholt-type diagrams ( $^{230}\text{Th}/^{232}\text{Th}$  vs.  $^{238}\text{U}/^{232}\text{Th}$ , and  $^{234}\text{U}/^{232}\text{Th}$  vs.  $^{238}\text{U}/^{232}\text{Th}$ , respectively; Figs. 5 and 6), which are in fact two dimensional slices of three dimensional  $^{238}\text{U}$ – $^{234}\text{U}$ – $^{230}\text{Th}$  diagrams. Both isochron types yield identical values for the authigenic and detritus components, although the Osmond-type diagrams provide a clearer assessment of the quality of the low- $^{232}\text{Th}$  authigenic samples (i.e., aragonite), while the Rosholt-type diagrams allow clearer evaluation of the high- $^{232}\text{Th}$  detritus-rich samples. The isochron diagrams have advantages over the single

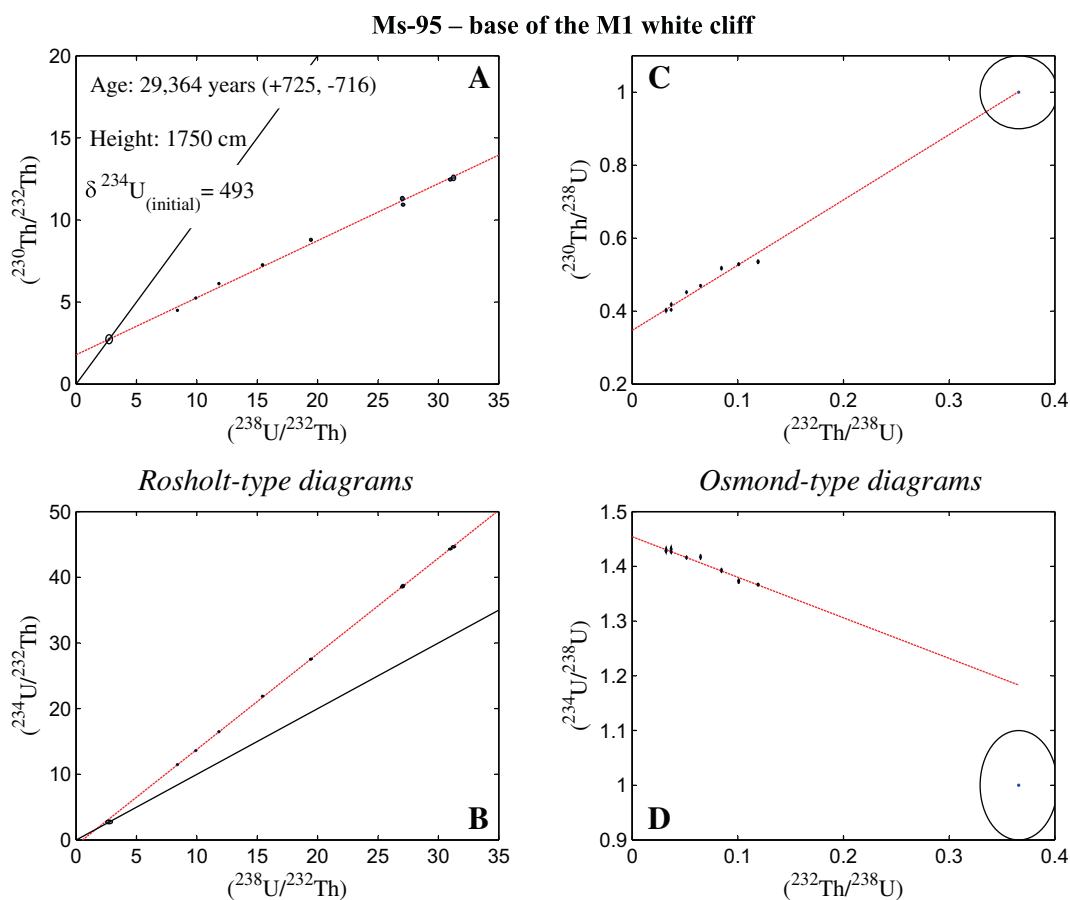


Fig. 5. U–Th isochron diagrams for sample set Ms-95 of M1. (A and B) “Rosholt-type” diagrams, (C and D) “Osmond-type” diagrams. Isochron ages used in this study are based on the Osmond-type diagram y-axis intercepts, which define the authigenic carbonate composition. The isochron cannot correct for the presence of a hydrogenous Th component (see text for details); hence, the final isochron age propagating this component is older by 530 years at 29,894 (+1299, –1290) years.

sample corrections when there is a significant variation in the mixing proportions of coeval detritus and carbonate samples, allowing extrapolation of the compositions of the detrital and authigenic phases (Kaufman, 1993; Ludwig and Titterton, 1994). Such a set of samples then shows a large range of either  $(^{232}\text{Th}/^{238}\text{U})$  ratios or  $(^{238}\text{U}/^{232}\text{Th})$  ratios, depending on whether Osmond-type or Rosholt-type isochrons are used, and the composition of the Detrital End Member (DEM) does not have to be explicitly determined (or assumed).

## 5.2. U–Th dating of the Lisan Formation

A detailed qualitative and quantitative study of U–Th dating of Lisan and Dead Sea sediments by Haase-Schramm et al. (2004) (termed hereafter: “H-S”) focused on the establishment of the chronology of a single stratigraphic section at the Perazim Valley (PZ1 section; Fig. 1). They corrected for the presence of detritus using a DEM composition of  $\text{Th}/\text{U}_{(\text{atomic})} = 0.85 (\pm 10\%)$ ,  $\text{U} = 4.26$  ppm, and  $(^{234}\text{U}/^{238}\text{U}) = 1$ , subtracting this from measured values when calculating single sample ages, and including it as

an isochron point when calculating isochron ages. They further corrected for initial hydrogenous Th based on the results of U–Th dating of a pristine modern aragonite sample with a negligible detrital matter content; for calculations of single sample ages this involved subtracting  $[\text{Th}] = 0.08$  ppm and  $^{232}\text{Th}/^{230}\text{Th}_{(\text{atomic})} = 44,000$  from measured values, and for isochrons it involved subtracting 340 years (Appendix A2 in H-S outlines a detailed correction procedure). Although the corrected U–Th ages were in good agreement with radiocarbon ages of organic debris recovered from the PZ1 section, some sets of coeval samples showed scatter beyond the analytical error, reflecting an additional natural geological variability of the U–Th system, possibly related to a varying composition of the DEM or hydrogenous component, or post-depositional overprinting. This excess scatter is expressed by a Mean Square Weighed Deviation (MSWD) value significantly higher than 1 in isochron diagrams.

In this work, recognizing the difficulty to determine a single basin-wide and time-constant DEM and hydrogenous correction procedure, we estimate the DEM composition for each individual set of coeval samples based on the intercept between the isochron curve and the secular equilibrium curve (i.e., the equiline in Rosholt-type diagrams

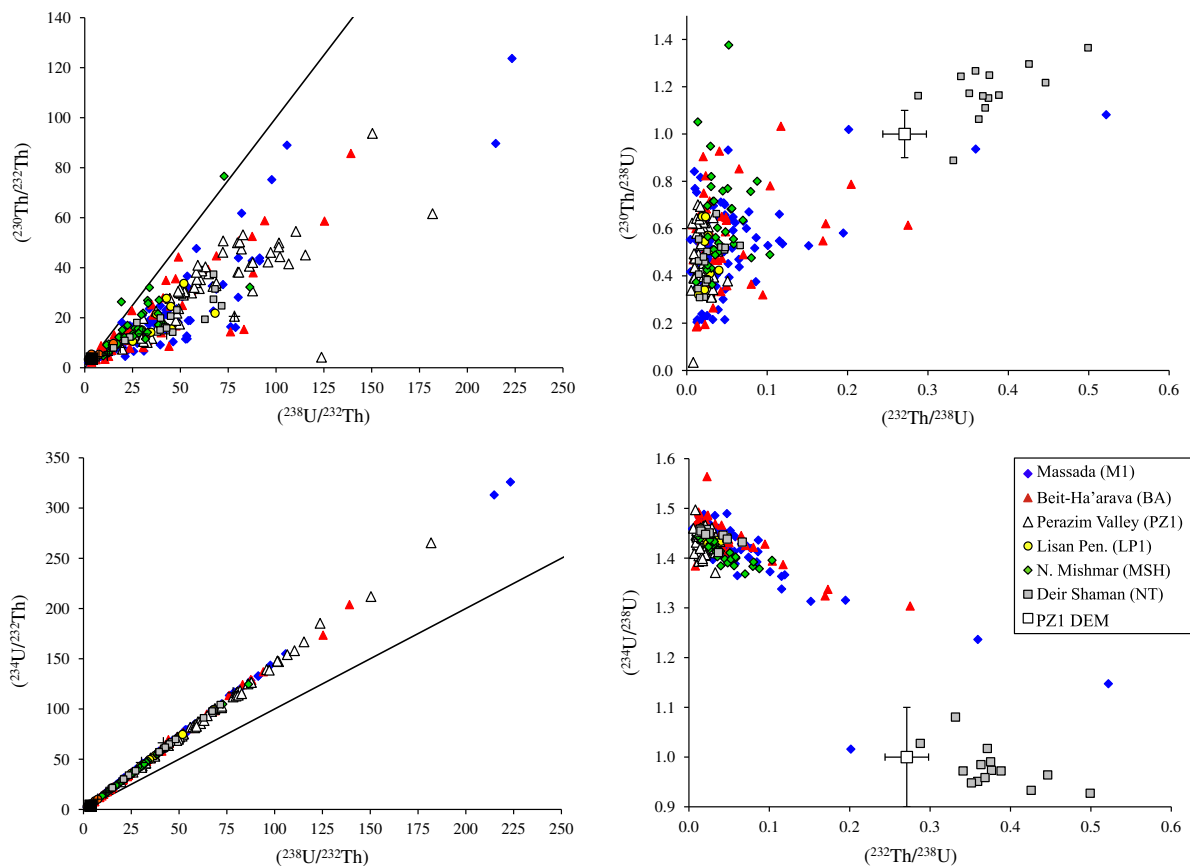


Fig. 6. Compiled U–Th isochron diagrams for the M1, Ba, PZ1, LP1, SH, and NT sections. For reference, a  $(^{232}\text{Th}/^{238}\text{U}) = 0.271 \pm 10\%$  is given as white square in two right panels, marking the DEM composition assumed by Haase-Schramm et al. (2004).

or an ordinate value of 1 in Osmond-type diagrams) under the premise that  $^{238}\text{U}$ ,  $^{234}\text{U}$  and  $^{230}\text{Th}$  are in secular equilibrium in detritus material. In well-established isochron sets, the DEM value and related uncertainty have little impact on the final isochron age (although they control the corresponding single sample age correction). Yet it is important to note that in many cases in which there are few measured authigenic samples, or they display limited  $^{238}\text{U}/^{232}\text{Th}$  variability (i.e., limited spread on the isochron diagram), or there are large analytical errors, the size of the uncertainty attributed to the DEM value has as much an effect on the isochron age calculation as the assumed DEM composition itself. This stems from the leverage of the DEM point on the isochron slope and intercept, which is inversely proportional to the assigned uncertainty when each sample is error weighted.

In order to estimate realistic age uncertainties we tested the effect of several DEM uncertainty values on the age calculations in two of the main sections discussed here, PZ1 and M1. Fig. 4 presents a summary of three of the procedures examined: (1) a 10% DEM uncertainty (used by H-S), (2) a 70% DEM uncertainty, (3) a 10% DEM uncertainty for the isochron calculation and a 30% DEM uncertainty for the single sample calculations. In procedures 2 and 3, the isochron uncertainties were further expanded by the square root of the MSWD, in order to account for

observed scatter that exceeds the analytical scatter (Wendt and Carl, 1991; Ludwig, 2003). The results imply that the sample uncertainties in procedures 1 and 2 are significantly under- and over-estimated, respectively, whereas procedure 3 provides a better prediction of the scatter of the samples about a linear age–height curve. The use of a smaller DEM uncertainty for isochron calculations compared to single sample calculations is required because large DEM uncertainties frequently result in unreasonably offset isochrons, due to the weaker leverage of the DEM data point. The expansion of the isochron uncertainties by the square root of the MSWD results in similar magnitude of uncertainties for single samples and their isochron age correction procedures.

Estimation of the composition of the hydrogenous Th in the samples is also challenging, although its effect on the age is far more limited than that of the DEM. We estimated the average age offset between samples where only detritus is assumed to be present and samples where both detritus and hydrogenous Th is assumed to be present, by calculating coupled sets ages in the two main sections discussed here (PZ1 and M1), following the procedures of H-S. Accordingly, the hydrogenous Th component imposes ages that are on average older by  $530 \pm 570$  years than ages where hydrogenous Th is not assumed. For comparison, our results are in reasonable agreement with those of H-

S, who based on a single test case sample, estimated that initial hydrogenous Th caused uncorrected ages to be too old by  $\sim 340$  years. It is worth noting that because each set of coeval samples in this study is assumed to contain a slightly different DEM, the effect of the hydrogenous Th correction is correspondingly different, and in many cases involves a correction toward an older age (rather than the more intuitive effect of a shift toward a younger age) because of the difference between the  $^{232}\text{Th}/^{230}\text{Th}$  ratio of the DEM and the hydrogenous component (as illustrated in Fig. 3 of H-S).

We acknowledge that some aspects of the correction procedures are determined somewhat arbitrarily, the linear age–height models are not necessarily continuous, and the DEM and hydrogenous Th compositions might change between sections and in different parts of an individual section. Yet the combined error propagation used here provides a conservative estimate of the true scatter of the sample ages.

## 6. RESULTS

### 6.1. U-decay series and supporting data

For this study, 211 samples were measured for their U and Th isotopic compositions. The results are tabulated together with age calculations and complementary mineralogical data in EA2 (M1 section,  $n = 91$ ), EA3 (LP1 section,  $n = 9$ ), EA4 (MSH section,  $n = 33$ ), EA5 (BA section,  $n = 47$ ) and EA6 (NT section,  $n = 31$ ). Detailed isochron diagrams for the M1, BA, MSH and PZ1 sections are given in Figs. 6, 7, and EA7–10.

Single sample age uncertainties reflect the analytical uncertainty, and corrected single sample age uncertainties

further propagate uncertainties related to the DEM. Average single sample ages are reported with a  $2\sigma$  standard error age uncertainty and isochron age uncertainties represent a 95% confidence limit.

### 6.2. Constructing preliminary U–Th-based age–height models

As discussed in Section 5.2, the measured composition of each sample is corrected for detritus U and Th, and hydrogenous Th. The DEM value is retrieved from the intercept of the isochron curve of coeval samples with a secular equilibrium value, and typically displays a range of  $6 > (^{238}\text{U}/^{232}\text{Th}) > 1$  (Fig. 8). This value is applied for the calculation of single sample and isochron ages assuming uncertainties of  $\pm 10\%$  and  $\pm 30\%$ , respectively. In single sample calculations the hydrogenous Th is corrected assuming a composition of  $[\text{Th}] = 0.08$  ppm and  $^{232}\text{Th}/^{230}\text{Th}_{(\text{atomic})} = 44,000$ . For isochron data sets, we assumed the effect of this component on the age to be  $+530$  ( $\pm 570$ ). In general, sets of coeval samples were rejected from being considered as isochrons if they consisted of less than three measured samples and they displayed negative extrapolated DEM ( $^{238}\text{U}/^{232}\text{Th}$ ) ratios.

Details of the development of preliminary age–height models for the individual sections are provided in the following section, and summarized in Fig. 9.

#### 6.2.1. Massada (M1)

At the Massada M1 section (Figs. 6, 7, and EA2,7), most sets of coeval samples yielded DEM values close to those used by H-S at PZ1 (Fig. 8) and resulting average single sample and isochron ages range between 75.95–12.56 and 68.05–13.89 ka, respectively.

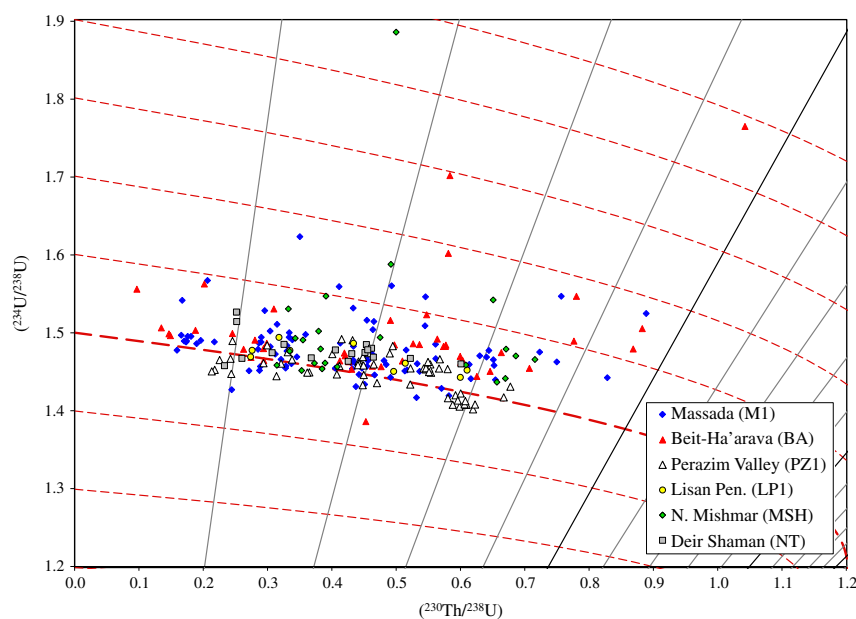


Fig. 7.  $(^{230}\text{Th}/^{238}\text{U})$  vs.  $(^{234}\text{U}/^{238}\text{U})$ . The dashed red curves represent the  $(^{234}\text{U}/^{238}\text{U})$  decay curves, and the thick curve in the middle reflects initial  $(^{234}\text{U}/^{238}\text{U}) = 1.5$ . Sub-vertical grey lines represent isochrons in 20 ka intervals; the black curve is the 100 ka isochron. Data points are corrected for the presence of detritus and hydrogenous Th (see text for details). Additional detritus samples (low  $^{234}\text{U}/^{238}\text{U}$ ) are not presented. (For interpretation of the references to color in this figure legend, the reader is referred to the web version of this article.)

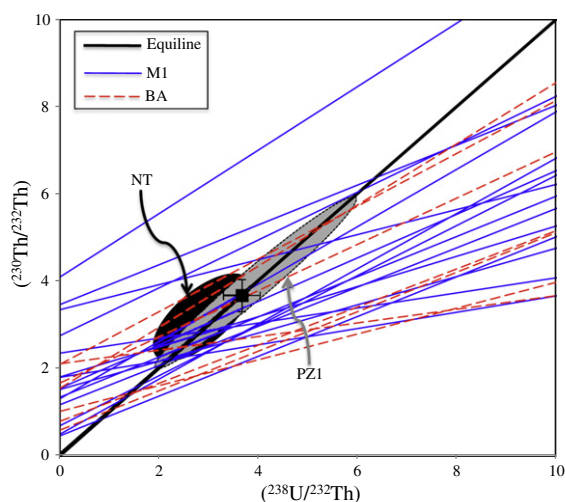


Fig. 8. High  $^{232}\text{Th}$  range of a compiled “Rosholt-type” isochron. The regression curves calculated at M1 and BA (blue and red curves, respectively), intercept the equiline near values of measured detritus samples from both sites, as well as from PZ1 and NT (black and grey ovals, respectively). The  $(^{238}\text{U}/^{232}\text{Th})_{\text{DEM}}$  value used by Haase-Schramm et al. (2004) is  $3.689 \pm 10\%$  (black rectangle), within error of the value of  $\sim 3.5$  proposed by Kaufman et al. (1992), and agrees well with the equiline-intercept points in the diagram. (For interpretation of the references to color in this figure legend, the reader is referred to the web version of this article.)

Because of inconsistencies in the apparent ages at some elevations of the M1 section, we further filtered the data by considering only data sets containing three or more measured samples, where the extrapolated DEM value yielded a positive  $(^{238}\text{U}/^{232}\text{Th})_{\text{DEM}}$  ratio (EA2). The filtered data is presented in Fig. 9B, where the Lower and Upper Members display overall stratigraphic order, while relative offsets toward young ages dominate the Middle Member interval. We calculated error-weighted linear regression curves based on isochron ages in the lower and upper parts of the sequence (between 0–1650 cm and 1750–2970 cm, respectively). The upper regression also considered the radiocarbon ages retrieved from organic material (Prasad et al., 2004). The average residual values for the regression curves are 4.5 ka and 2.2 ka, respectively. The lower regression curve implies a basal age of 66.36 ka, an LGU age in the range of 59.52–57.12 ka, and a Small Gypsum Unit age in the range of 55.14–52.85 ka, all in good agreement with stratigraphic counterparts at PZ1 (Table 2).

The upper regression curve yields regression ages for the base of the White Cliff (above the Broken Gypsum Unit, 17.05 m), the UGU (26.23–28.13 m) and the Additional Gypsum Unit (29.30–29.70 m) of 30.10, 17.73–15.17, and 13.60–13.06 ka, respectively.

### 6.2.2. Lisan Peninsula (LP1)

The Lisan Peninsula LP1 section, whose base is at 374 m-bmsl, was first described by Bartov (1999). It is overall similar to the Lisan section at Massada (M1) and comprises pristine *aad* bundles and intermittent gypsum beds. The sampling resolution of the LP1 section is low compared

to the other sections discussed here, reflecting limited accessibility to this area. Nevertheless, the stratigraphic correlation of the major gypsum units provides robust age–height constraints, which are complemented by several U–Th ages that display stratigraphic order (except for one outlier) and are in good agreement with the ages established for the other sites (Fig. 9A). Because none of the coeval sample sets contained more than two single samples (EA3), we did not calculate an extrapolated DEM value for each, nor did we discriminate against these samples, as was the approach at M1. Ages were calculated using a DEM Th/U atomic ratio of 0.85 (following H-S).

The capping sediments of the Lisan Formation over most of the Lisan Peninsula are comprised of a gypsum bed that corresponds stratigraphically with the Broken Gypsum Unit identified at M1. It is thus noteworthy that over most of the Lisan Peninsula, the post-38 ka Lisan deposits are not present, despite their presence in other sections at higher elevations, and therefore they have been eroded. This relationship is interpreted to reflect transgressive erosion, as explained in Section 6.2.6.

### 6.2.3. Nahal Mishmar (MSH)

The Nahal Mishmar (MSH) section is located  $\sim 5.5$  km north of the M1 section (Fig. 1), and is similarly dominated by aragonite and gypsum. The MSH section is capped by a gypsum layer at 17.2 m, which correlates stratigraphically to the Broken Gypsum Unit at M1. The absence of the sedimentary sequence above the Broken Gypsum Unit implies significant sediment removal from this site, despite the high stand conditions that prevailed in the subsequent history of Lake Lisan.

U–Th ages determined in this section are few and scattered. The four-isochron sets that passed the same filtering parameters used for M1 (EA4) define an error-weighted regression curve with a large average residual (7.24 ka; Table 2), and anchor point ages that are considerably younger compared to other sections (Figs. 9F and 10). As a result, while the Nahal Mishmar site provides complementary stratigraphic constraints, the age data is not used for determination of the ages of the anchor-points in the Lisan Formation.

### 6.2.4. Beit-Ha’arava (BA)

The Beit-Ha’arava (BA) section, located at the northern tip of the Dead Sea (Fig. 1), is dominated by aragonite and gypsum, and contains most of the major gypsum units identified at Massada. We measured and calculated U–Th ages for 47 samples from 11 elevation points, yielding isochron and average single sample ages in the range of 96.38–12.37 ka and 82.79–11.81 ka, respectively (EA5,8). Similar to the approach at M1, we filtered the data by considering only data sets containing three or more coeval samples, where  $(^{238}\text{U}/^{232}\text{Th})_{\text{DEM}} > 0$  (EA5). The results yield an overall reasonable stratigraphic order with no field evidence for sedimentary unconformities. An error-weighted linear regression is unreasonably biased toward old ages at the lower part of the section and we therefore calculate a simple linear regression curve for the entire section (Fig. 9C) yielding good agreement with ages of correspond-

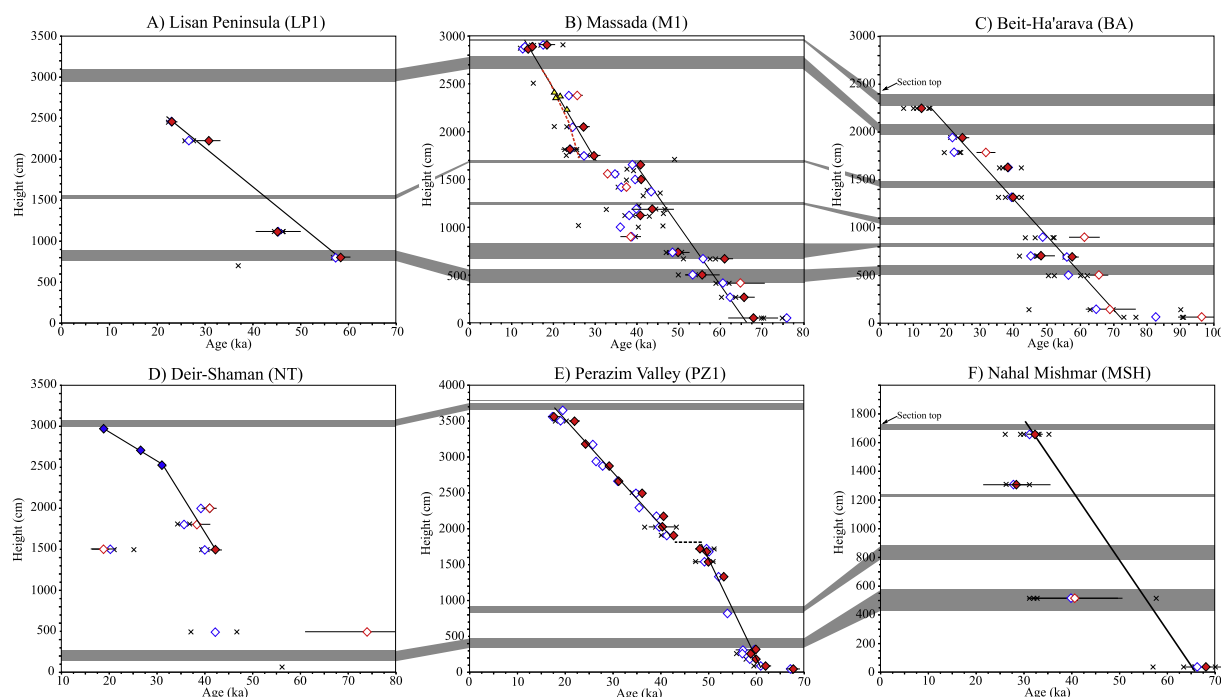


Fig. 9. Preliminary age–height models. Age–height models were developed for all the sites by filtering the measured ages (explained in the text) in order to calculate error-weighted linear regressions for segments of each section. Isochron ages that were used are full red diamonds. Empty red and blue diamonds mark isochron and average single samples, respectively, that were not used. Black crosses mark single sample ages. At M1, the regression for the upper part of the section includes  $^{14}\text{C}$  ages of organic material (yellow triangles; Prasad et al., 2004) and aragonite laminae (empty triangles; this work). At NT, the regression for the upper part of the section is based on three single sample ages (full blue diamonds). Grey horizontal shades mark stratigraphic horizons that can be correlated between the sections. (For interpretation of the references to color in this figure legend, the reader is referred to the web version of this article.)

ing layers at the other sites discussed here (Table 2 and Fig. 10).

#### 6.2.5. Deir-Shaman (NT)

The Deir-Shaman NT section is located at the central part of the Jordan valley (Fig. 1), about  $\sim 85$  and  $\sim 105$  km north of M1 and PZ1, respectively. The section base at 369 m-bmsl (Waldmann et al., 2009) is only slightly higher than the base of the M1 section. The only stratigraphic tie-points exposed at this section are the LGU and UGU (Figs. 3 and 9D).

Seventeen aragonite samples from nine stratigraphic levels and 14 detritus samples were separated from the NT section for U–Th isotope analyses (EA6). The large number of detritus samples constrains the DEM composition at this location to  $(^{238}\text{U}/^{232}\text{Th}) \approx 3.5$ , similar to PZ1 (Fig. 8), and despite the long distance between them.

The age–height model for the White Cliff at the NT site was constructed by calculating an error-weighted linear regression based on three single sample ages between 25 and 30 m. The results indicate ages between 31.02 ka at the base of the White Cliff and 18.85 ka below the UGU, which are equivalent to the age of the White Cliff at M1 (30.10–17.7 ka). Sediments overlying the UGU display a gradual transition over  $\sim 3$  m from an *aad* facies to surface cover soil. The underlying sediments between 14.9 and 25.2 m are comprised of alternating packages of marl and *aad*. Because simple and error-weighted regression curves

are unreasonably offset in this part of the section we tentatively use a linear regression between two points at 14.9 and 25.25 m, using ages of 42.27 and 31.02 ka, respectively. These ages correspond to a robust isochron age (at 14.9 m) and the calculated regression age for the base of the White Cliff. The age anchor at 14.9 m was chosen because this point is located above a prominent beach bar indicating preceding low stand conditions, most likely corresponding to a significant sedimentary hiatus identified at PZ1 between  $\sim 49$  and 44 ka (H-S). Though the resulting regression curve is deemed reasonable because it generally fits the data in this interval, the age model will be refined in a later part of the discussion based on stratigraphic–limnologic considerations pertaining to the occurrence of the three Middle Member Aragonite Units (MMAU) in this section. No reliable U-series ages are available for the lower part of the section.

#### 6.2.6. A transgressional hiatus at M1 between 38 and 31 ka?

A noticeable age discrepancy is revealed across the Broken Gypsum Unit at M1, where a gap of about 7 ka separates the ages extrapolated from the lower and upper regression curves ( $\sim 38$  and 31 ka, respectively; Fig. 9B). This gap is supported by the discrepancy between two different sets of coeval samples, immediately below and above the Broken Gypsum Unit (*Ms-VI* and *Ms-95*, respectively; EA2), both yielding robust isochron ages ( $40.93 \pm 1.04$  and  $29.89 \pm 1.29$  ka, respectively).

Table 2  
Event anchor ages.

	Additional Gypsum Unit		UGU		Broken Gypsum Unit		Curled Gypsum Unit		Small Gypsum Unit		LGU		Lisan Base
	Top	Bottom	Top	Bottom	Top	Bottom	Top	Bottom	Top	Bottom	Top	Bottom	
<i>Regression ages</i>													
M1	13.06	13.60	15.17	17.73		38.68	45.81	46.12	52.85	55.14	57.12	59.52	66.36
Uncertainty	2.20	2.20	2.20	2.20		3.50	3.50	3.50	3.50	3.50	3.50	3.50	3.50
PZ1		14.60	15.00	17.40		39.90			54.40	54.90	57.20	58.20	69.20
Uncertainty		0.81	0.81	0.81		0.81			0.82	0.82	0.82	0.82	0.82
BA		15.21	17.24	22.54		36.83	45.02	46.47	51.89	52.85	57.94	60.42	73.52
Uncertainty		3.44	3.44	3.44		3.44	3.44	3.44	3.44	3.44	3.44	3.44	3.44
NT			15.86	18.10									
Uncertainty			0.32	0.32									
Error-weighted mean	13.06	14.46	15.67	18.15		39.67	45.41	46.30	53.75	54.61	57.31	58.77	69.45
Sterr	2.20	0.47	0.51	1.21		0.61	0.40	0.17	0.73	0.73	0.26	0.64	2.08
<i>Supporting ages</i>													
LP1				13.44								56.53	
Uncertainty				2.42								2.42	
MSH						32.08	41.02	41.47	48.88	49.63	54.25	57.33	65.96
Uncertainty						7.24	7.24	7.24	7.24	7.24	7.24	7.24	7.24
Tuned ages		<b>14.5</b>	<b>15.5</b>	<b>17.1</b>	<b>38.3</b>	<b>39.7</b>	<b>47.5</b>	<b>49.0</b>	<b>54.0</b>	<b>56.0</b>	<b>58.5</b>	<b>61.0</b>	
Uncertainty		0.5	0.5	0.5	0.5	0.5	0.5	0.5	0.5	0.5	1.0	1.0	

Comments: (1) Ages for PZ1 are from Haase-Schramm et al. (2004). (2) Uncertainties reflect the average residual value of radiometric ages around linear regression curves for each segment. (3) The above "event" ages are used to calculate and error-weighted mean age for each event. Due to scarce data points and little stratigraphic constraints, the data from LP1 and MSH is not used in the calculation. (4) Given the close coincidence between the Lisan "event" ages and occurrence of Heinrich events we tune the Lisan anchor ages to those of Heinrich events determined in Chinese cave deposits (following Wang et al., 2001).

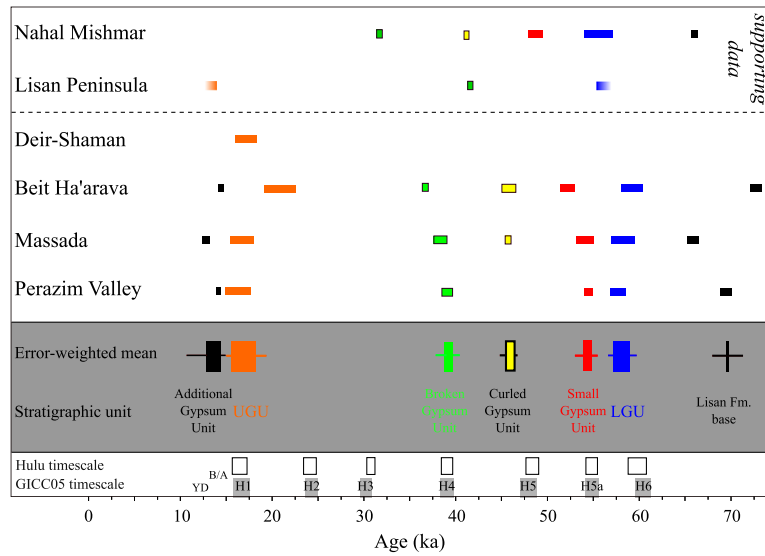


Fig. 10. Compiled event ages. The ages for stratigraphic tie points based on the filtered U–Th and  $^{14}\text{C}$  data are compared. At LP1, the low resolution of the columnar section and scarcity of samples, together with the systematic offset of ages at MSH, lead us to reject the ages from these two sections and only use them for complementary stratigraphic constraints. Most of the event ages in the different sections are in good agreement. An error-weighted mean age was calculated using the ages from each section (Table 2). The timing of the stratigraphic tie-points appear to coincide with the timing of prominent North Atlantic cooling perturbations during Heinrich stadials. In addition, Lake Lisan's water level reconstruction (Bartov et al., 2003) exhibits catastrophic lake level drops coinciding with Heinrich events. The timing of Heinrich stadials is shown for reference at the bottom (Wang et al., 2001; Wolff et al., 2010).

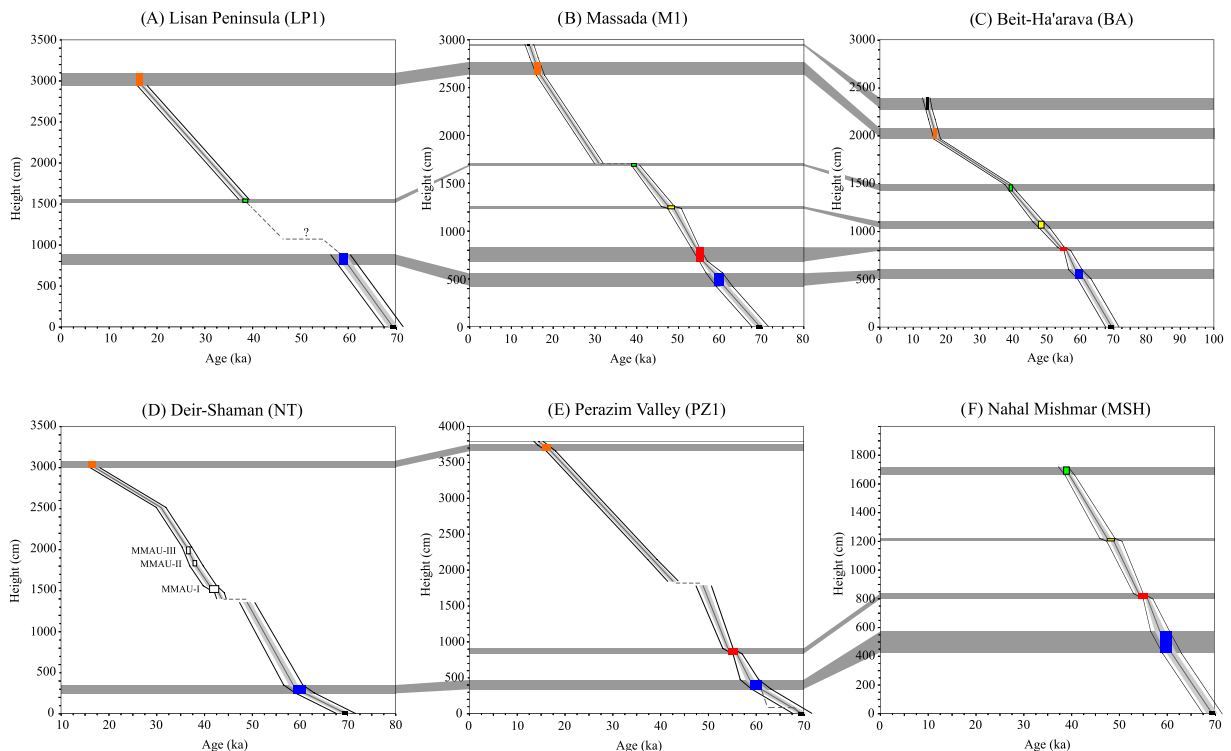


Fig. 11. Final age–height models. Ages of the Lisan anchor events are tuned to Heinrich events and integrated into the age–height models to produce final results. The color code for the anchors follows Fig. 10, where the lower black marker is the base of the Lisan Formation ( $69.5 \pm 1.0$  ka), blue is the LGU ( $61\text{--}58.5 \pm 1.0$  ka), red is the Small Gypsum Unit ( $56\text{--}54 \pm 0.5$  ka), yellow is the Curled Gypsum Unit ( $49\text{--}47.5 \pm 0.5$  ka), green is the Broken Gypsum Unit ( $39.7\text{--}38.3 \pm 0.5$  ka), orange is the UGU ( $17.1\text{--}15.5 \pm 0.5$  ka), and the upper black marker is the Additional Gypsum Unit ( $14.5 \pm 0.5$  ka). Uncertainties reflect the 68% (light grey shadow) and 95% confidence limit, calculated using the  $P$ -Sequence procedure in Oxcal v4.1 (Bronk Ramsey, 2009). An alternative age model at the base of the PZ1 section (E) is given as dashed curve. (For interpretation of the references to color in this figure legend, the reader is referred to the web version of this article.)

Hence, despite a lack of supporting field evidence, a significant hiatus between the Broken Gypsum Unit at  $\sim 38$  ka and the base of the White Cliff (Upper Member) at  $\sim 31$  ka is revealed. During the same time period, deposition continued at the shallower PZ1 section, indicating that this was not a continuously low lake level period. We suggest that the missing sedimentary sequence above the Broken Gypsum Unit at M1 (that is, those sediments deposited between  $\sim 38$  and  $31$  ka) was removed by *transgressional erosion*, whereby a lake level-rise at  $\sim 31$  ka eroded the section at M1 down to the  $\sim 38$  ka Broken Gypsum Unit. The relatively rigid gypsum layer limited the base of this sediment truncation. Transgressional erosion was similarly suggested by Bartov (2004) for the truncation of the upper part of the Lisan Formation exposed at the Lisan Peninsula (Fig. 1), where most of the surface is composed of a thick gypsum layer correlating to the Broken Gypsum Unit at Massada. In addition, the Lisan Formation exposed at the MSH section is truncated above the Broken Gypsum Unit, and at the NT section, the base of the *aad* sequence comprising the White Cliff is well constrained to  $\sim 31$  ka. Both latter observations support the occurrence of a transgressional erosion event due to a sharp lake level rise at about  $31$  ka that removed large parts of the Lisan sediments.

#### 6.2.7. The age of the Additional Gypsum Unit (AGU)

Isolated remnants of sediments associated with the Lisan Formation that are younger than the UGU are exposed at the M1, PZ1, NT and BA sections. At M1, they comprise  $\sim 1.16$  m of *aad* capped by a  $\sim 40$  cm thick laminated gypsum dubbed the Additional Gypsum Unit (AGU). A similar

structure exists at BA, where a brown silt layer, rather than gypsum, caps the *aad*. At NT, the sediments above the UGU shift gradually over  $\sim 3$ – $4$  m from aragonite laminae intercalating with marls to a soil cover. The pre-tuning age range for the AGU is  $14.46$ – $13.06$  ka, when global climate had already shifted greatly from a glacial mode to an interglacial one and thus cannot be a priori considered in the same terms as the glacial-type gypsum – Heinrich association. The stratigraphic structure of the AGU capping an *aad* interval, marks a dry spell at the end of a wet phase that correlates with the lake rise after the deposition of the UGU and its fall during the Bølling/Allerød warming (B/A;  $14.7$ – $12.9$  ka). Thereafter, the lake rose again during the Younger Dryas cooling (YD;  $12.9$ – $11.5$  ka, Stein et al., 2010). Current age uncertainties are too large to confidently determine the climatic context and age of the AGU, warranting further consideration as improved ages of this part of the section become available. For the purpose of the discussion in the main text, we tentatively use an age of  $14.5 (\pm 0.5)$  ka as the deposition age of the base of the AGU.

## 7. DISCUSSION

### 7.1. Lake Lisan chronology

#### 7.1.1. Event-based unified chronology

The basin wide stratigraphic tie-points, combined with the independent age constraints for each of the studied Lisan sections, allow construction of a unified chronological framework for Lake Lisan. Fig. 10 presents a comparison of the site-specific ages for the most prominent gypsum

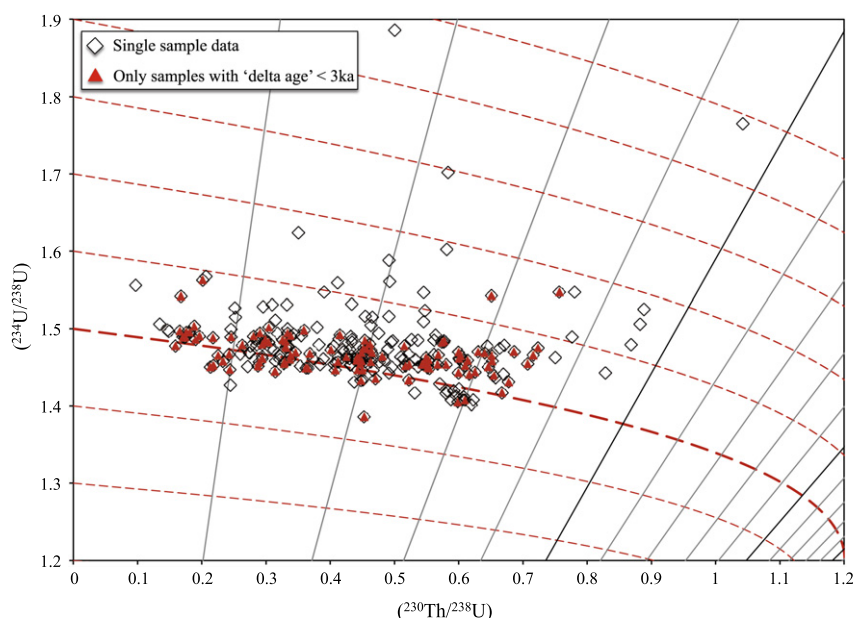


Fig. 12.  $(^{230}\text{Th}/^{238}\text{U})$  vs.  $(^{234}\text{U}/^{238}\text{U})$ . Empty diamonds are the data from all sites in this study (corresponding to the data in Fig. 7) and red triangles mark samples displaying ‘delta age’ values lower than  $3$  ka (where ‘delta age’ is the age difference between the U–Th based age of a sample and the regression age determined for the same elevation). Applying the ‘delta age’ filter results in convergence of data toward a narrow average initial  $(^{234}\text{U}/^{238}\text{U})$  of  $1.521 \pm 0.030$  ( $1\sigma$ ), compared to the total average value of  $1.550 \pm 0.178$  (excluding detritus samples displaying initial  $(^{234}\text{U}/^{238}\text{U}) < 1.4$ ). This pattern suggests the authigenic Lisan aragonites have a near constant initial  $(^{234}\text{U}/^{238}\text{U})$  composition and that deviations are the result of detrital contamination or diagenetic alteration. (For interpretation of the references to color in this figure legend, the reader is referred to the web version of this article.)

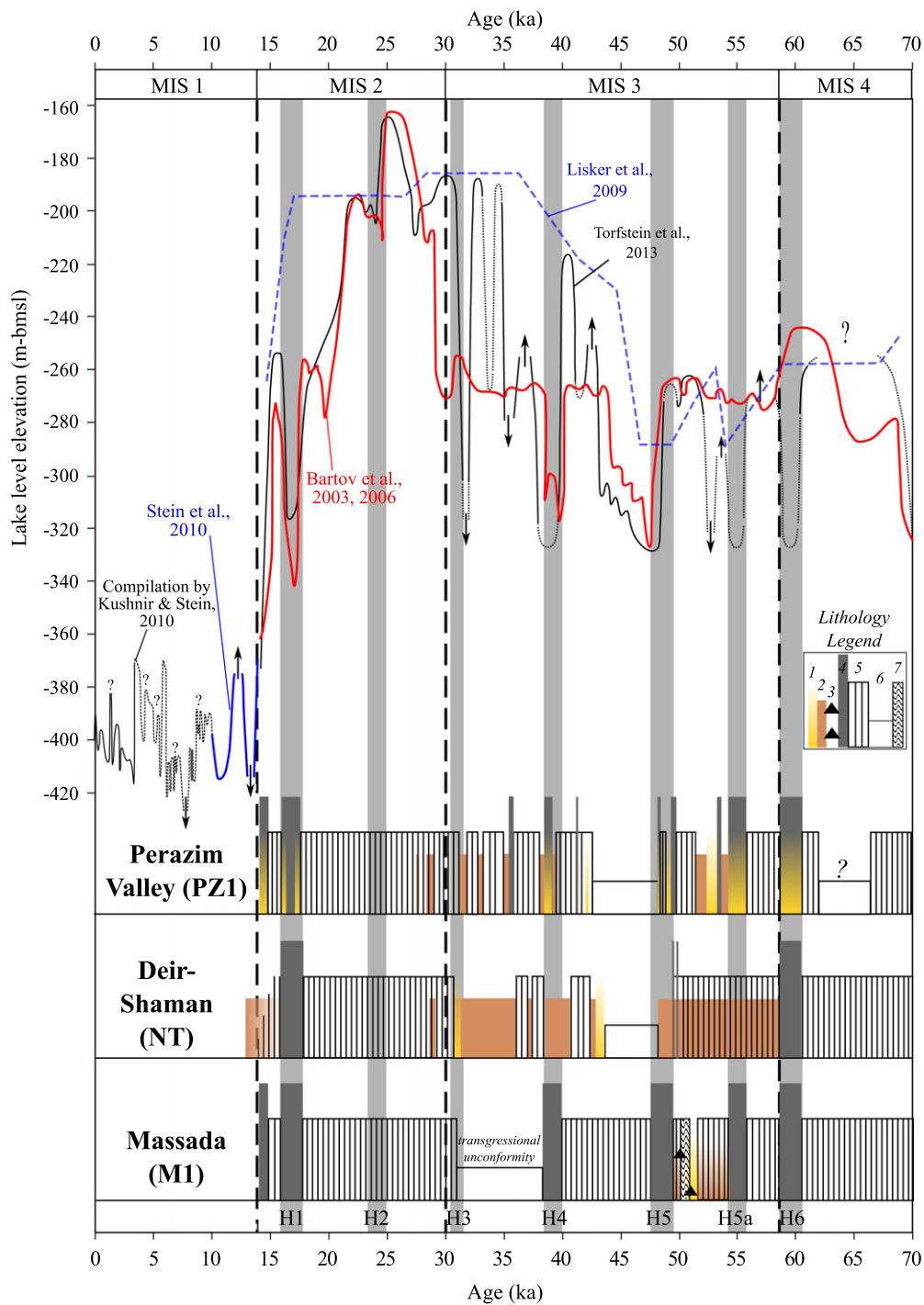


Fig. 13. Lisan sedimentary sections and lake level reconstructions. The lithology of three representative sections (M1, NT, and PZ1) is plotted vs. age, according to the unified Lisan chronology, and compared to lake level reconstructions. All sites indicate high-stand conditions during most of MIS4 and MIS2, both of which terminated with the deposition of massive gypsum units. Frequent oscillations in the lithology are observed during warmer and dryer MIS3. The frequency of fluctuations is higher in the marginal sections (e.g., NT, PZ1), while the deeper-lake M1 section is characterized by shifts between alternating aragonite–detritus (*aad*) couplets and gypsum layers. The gypsum layers correspond to the timing of Heinrich events in the North Atlantic, marked by vertical grey bars (Wang et al., 2001) timescales. During the Pleistocene–Holocene transition, the lake receded and all sections were exposed. For clarity, the high-resolution details of the Gypsum Units are not presented. Legend abbreviations: (1) sand, (2) marl, (3) halite, (4) gypsum, (5) *aad*, (6) hiatus, (7) convolute unit (see text for details).

units. Neglecting the few ages from MSH and LP1, we used the regression ages at each site to calculate an error-weighted average age for the base of the Lisan Formation

(69.45 ± 2.08 ka), the Lower Gypsum (58.77–57.31 ka), Small Gypsum (54.61–53.75 ka), Curled Gypsum (46.30–45.41 ka), Broken Gypsum (basal age of 39.67 ± 0.61 ka),

Table 3  
Summary of unified chronology ages for M1 section.

Stratigraphy	Samples	Height (cm)	Tuned anchor age (ka)	Regression age (ka)	Uncertainty (ka)	Regression age equation	Sedimentation rate (cm/ka)
<i>Upper member</i>							
Additional Gypsum Unit (base)		2930	<b>14.50</b>		0.5	$T = (4626.5 - H)/117$	117.0
Upper Gypsum Unit (top)		2813	<b>15.50</b>		0.5	$T = (4653.6 - H)/118.8$	118.8
Upper Gypsum Unit (base)		2623	<b>17.10</b>		0.5	$T = (3752.3 - H)/66$	66.0
	Ms100	2050		25.78	0.5		66.0
	Ms90	1813		29.36	0.5		66.0
	Ms95	1750		30.32	0.5		66.0
Base of white cliff		1705	<b>31.00</b>		0.5		
<i>Middle Member</i>							
Broken Gypsum Unit (base)		1690	<b>39.70</b>		0.5	$T = (3904 - H)/55.8$	55.8
	Ms-VI	1618		40.99	0.5		55.8
	Ms-V-22-21	1488		43.32	0.5		55.8
	Ms-III-33	1356		45.69	0.5		55.8
Curled Gypsum Unit (top)		1255	<b>47.50</b>		0.8	$T = (1856.7 - H)/12.7$	12.7
Curled Gypsum Unit (base)		1236	<b>49.00</b>		0.8	$T = (5263.8 - H)/82.2$	82.2
	Ms-II	1166		49.85	0.7		82.2
Convolute Unit (top)		1115		50.47	0.7		82.2
Convolute Unit (base)		1016		51.68	0.6		82.2
Pebble unit		1000		51.87	0.6		82.2
Small Gypsum Unit (top)		825	<b>54.00</b>		0.5	$T = (4605 - H)/70$	70.0
Small Gypsum Unit (base)		685	<b>56.00</b>		0.5	$T = (3373 - H)/48$	48.0
<i>Lower Member</i>							
Lower Gypsum Unit (top)		565	<b>58.50</b>		1.0	$T = (4004.8 - H)/58.8$	58.8
Lower Gypsum Unit (base)		418	<b>61.00</b>		1.0	$T = (3414.2 - H)/49.1$	49.1
	Ms-8	415		61.06	1.0		49.1
	Ms-5	266		64.09	1.0		49.1
	Ms-3	50		68.49	1.0		49.1
Base of section		0	<b>69.51</b>		1.0		

*Comments:* In the regression age equation,  $T$  stands for age (ka) and  $H$  stands for height (cm) (here and in the following tables). Uncertainty reported at 68% confidence limit.

Upper Gypsum (18.15–15.67 ka), and Additional Gypsum (14.46–13.06 ka) units (Table 2). The complications associated with the Broken Gypsum interval at M1, where a major transgression hiatus offsets ages below and above the unit, propagates some additional uncertainty into the determination of the age of this unit. Yet the stratigraphic correlation between this unit at M1 and an equivalent detritus–gypsum interval at PZ1, which was previously dated by H-S to 39.9–38.5 ka, lends further confidence in our age determination of this unit.

Excluding the AGU age (see Section 6.2.7), all the above ages are consistent, within error, with the timing of Heinrich stadials, when massive icebergs were discharged into the North Atlantic (Wang et al., 2001; Hemming, 2004). Supporting independent linkage between Heinrich events and Lake Lisan emerges from the Lisan lake level reconstruction (Bartov et al., 2003, 2006), where catastrophic lake level drops coincide with the timing of Heinrich events (Figs. 10 and 13). One of the most significant lake level drops took place at ca. 49 ka, in coincidence with the timing of H5, but about 3 ka older than our U–Th-based estimate of the age of the corresponding Curled Gypsum unit. Given the frequently observed age scatter below and above this gypsum unit, it is reasonable to infer that its deposition is

associated with the lake level drop. Thus, we tune the ages of the Lisan gypsum units to those of Heinrich events, using 61–58.5 ( $\pm 1$ ), 56–54 ( $\pm 0.5$ ), 49–47.5 ( $\pm 0.8$ ), 39.7–38.3 ( $\pm 0.5$ ), and 17.1–15.5 ( $\pm 0.5$ ) ka for H6, H5, H5a, H4 and H1, respectively (following Wang et al., 2001). This tuning step assumes a negligible time lag between the timing of Heinrich events in Hulu Cave and Lake Lisan; the attributed age uncertainties reflect the combined propagation of the possible time lag and the uncertainties in determining the precise timing of Heinrich events from Hulu Cave speleothems (Wang et al., 2001). This step finalizes the construction of a unified basin-wide chronology and allows us to establish high-resolution age–height models for each of the sections studied here, and elsewhere. Bayesian age–height models were applied at each of the sites on the basis of the anchors’ age–height details. The age–height models were calculated using the *P\_Sequence* function (assuming  $k$  factor of 1) in the Oxcal v4.1 program (Bronk Ramsey, 2009) and yield uncertainties between  $\sim 2000$  and 1000 years (95% confidence limit) at the base and top of the Lisan Formation, respectively (Fig. 11 and Tables 3–8).

In contrast to the gypsum-related “dry events”, the three MMAUs at Deir-Shaman represent wet perturbations during MIS3, when climate is overall warmer and drier than MIS2

Table 4  
Summary of unified chronology ages for PZ1 section.

Stratigraphy	Samples	Height (cm)	Tuned anchor age (ka)	Regression age (ka)	Uncertainty (ka)	Regression age equation	Sedimentation rate (cm/ka)
<i>Upper Member</i>							
Top of section		3785	<b>14.50</b>		0.5	$T = (4495.5 - H)/49$	49.0
Upper Gypsum Unit (top)		3736	<b>15.50</b>		0.5	$T = (4462.6 - H)/46.9$	46.9
Upper Gypsum Unit (base)		3661	<b>17.10</b>		0.5	$T = (4886.2 - H)/71.7$	71.7
	PZ1-3558	3558		18.54	0.5		71.7
	PZ1-3497	3497		19.39	0.5		71.7
	PZ1-3175	3175		23.88	0.5		71.7
	L21	2939		27.18	0.5		71.7
Clastic		2902		27.69	0.5		71.7
Clastic		2839		28.57	0.5		71.7
Clastic		2817		28.88	0.5		71.7
<i>Middle Member</i>							
Clastic		2630		31.49	0.5		71.7
Clastic		2495		33.37	0.5		71.7
	PZ1-2489	2489		33.46	0.5		71.7
		2410		34.56	0.5		71.7
Clastic		2351		35.38	0.5		71.7
	PZ1-2290	2290		36.23	0.5		71.7
	PZ1-2172	2172		37.88	0.5		71.7
Clastic (eq. to Broken Gypsum)		2142	<b>38.30</b>		0.5	$T = (4768.3 - H)/68.6$	68.6
Clastic (eq. to Broken Gypsum)		2046	<b>39.70</b>		0.5	$T = (4886.2 - H)/71.7$	71.7
	L9	2020		40.00	0.5		71.7
Clastic		1995		40.35	0.5		71.7
Clastic		1943		41.08	0.5		71.7
<i>Laschamp geomagnetic event</i>	PZ1-1900	1900		41.68	0.5		71.7
		1800		43.07	0.5		71.7
Hiatus (end)		1770		43.49	0.5		71.7
Hiatus (begin)		1770	<b>49.00</b>		0.8	$T = (10217 - H)/172.4$	172.4
	PZ1-1715	1715		49.32	0.8		172.4
	PZ1-1680	1680		49.52	0.8		172.4
Clastic		1622		49.86	0.7		172.4
Clastic		1547		50.29	0.7		172.4
Clastic		1294		51.76	0.6		172.4
Lisan geomagnetic event (?)		1200		52.31	0.6		172.4
Clastic		1172		52.47	0.6		172.4
Clastic		1158		52.55	0.6		172.4
Clastic + thin gypsum (eq. to Small Gypsum)		908	<b>54.00</b>		0.5	$T = (3041 - H)/39.5$	39.5
Clastic + thin gypsum (eq. to Small Gypsum)		829	<b>56.00</b>		0.5	$T = (8982.6 - H)/145.6$	145.6
<i>Lower Member</i>							
LGU (top)		465	<b>58.50</b>		1.0	$T = (3436.8 - H)/50.8$	50.8
LGU (base)		338	<b>61.00</b>		1.0	$T = (2760.8 - H)/39.7$	39.7
	PZ1-314	314		61.60	1.0		39.7
	PZ1-178	178		65.03	1.0		39.7
Hiatus (end)		60		68.00	1.0		39.7
Base of section		0	<b>69.51</b>		1.0		

*Comments:* The age tuning of the lower part of the section was minor compared to U–Th chronology, and we used an anchor age of  $49 \pm 0.8$  ka for an elevation of 17.70 m, corresponding with the regression age of H–S. U–Th dating below the LGU indicate a sedimentary hiatus, leading H–S to suggest two alternative age–height models for this interval. We used a linear age–height regression and refer the readers to H–S for further details about the alternative age model. Similarly, between 17.7 and 20.46 m (between the hiatus and the layer equivalent to Broken Gypsum Unit) we use a sedimentation rate of 71.7 cm/ka, corresponding to values calculated above this interval. The age at the top of the section is extrapolated from the UGU interval age equation. Uncertainty reported at 68% confidence limit.

Table 5  
Summary of unified chronology ages for NT section.

Stratigraphy	Samples	Height (cm)	Tuned anchor age (ka)	Regression age (ka)	Uncertainty (ka)	Regression age equation	Sedimentation rate (cm/ka)
<i>Upper Member</i>							
Upper Gypsum Unit (base)		3000	<b>17.10</b>		0.5	$T = (3590.5 - H)/34.5$	34.5
	NT-5	2970		17.97	0.5		34.5
	NT-31-B-1	2715		25.35	0.5		34.5
	NT-29	2525		30.86	0.5		34.5
Base of white cliff		2520	<b>31.00</b>		0.5	$T = (5439.7 - H)/94.2$	94.2
<i>Middle Member</i>							
MMAU-III (top)		2027	<b>36.23</b>	<i>36.50</i>	0.5	$T = (6009.1 - H)/109.9$	109.9
MMAU-II (base)		1800	<b>38.30</b>	<i>39.03</i>	0.7	$T = (5151 - H)/87.5$	87.5
MMAU-I (top)		1557	<b>41.08</b>	<i>41.74</i>	0.7	$T = (3203.6 - H)/40.1$	40.1
MMAU-I (base)		1477	<b>43.07</b>	<i>42.63</i>	0.5	$T = (9398.3 - H)/183.9$	183.9
Above beach-bar		1400	<b>43.49</b>		0.5		
Below beach-bar		1350	<b>49.00</b>		0.8	$T = (6492.4 - H)/104.9$	104.9
<i>Lower Member</i>							
Lower Gypsum Unit (top)		353	<b>58.50</b>		1.0	$T = (2646.2 - H)/39.2$	39.2
Lower Gypsum Unit (base)		255	<b>61.00</b>		1.0	$T = (2082.8 - H)/30$	30.0
Base of section		0	<b>69.51</b>		1.0		

*Comments:* Regression ages of the MMAU units (italicized font) were calculated based on an interpolation between anchor ages at 25.2 m (31 ka) and 14.0 m (43.49 ka). These ages are further refined by wiggle matching to regression ages of aad intervals in the PZ1 section, and are presented as the tuned anchor ages for the MMAU units with attributed upper boundary uncertainties reflecting the maximum shift between regression and tuned ages or the corresponding uncertainty at PZ1, the higher one of the two. MMAU-I is assumed to be synchronous with an aad package at PZ1 between 18 and 19.43 m (43.07–41.08 ka), and MMAU-II and III are assumed to display two sub-intervals within the time window represented by an aad package at PZ1 from 21.42 to 22.90 m (38.3–36.23 ka). Uncertainty reported at 68% confidence limit.

Table 6  
Summary of unified chronology ages for BA section.

Stratigraphy	Height (cm)	Tuned anchor age (ka)	Regression age (ka)	Uncertainty (ka)	Regression age equation	Sedimentation rate (cm/ka)
<i>Upper Member</i>						
Additional Gypsum Unit (base of silt)	2285	<b>14.50</b>		0.5	$T = (3836.5 - H)/107$	107.0
Upper Gypsum Unit (top)	2178	<b>15.50</b>		0.5	$T = (4163.9 - H)/128.1$	128.1
Upper Gypsum Unit (base)	1973	<b>17.10</b>		0.5	$T = (2360.2 - H)/22.6$	22.6
<i>Middle Member</i>						
Broken Gypsum Unit (top)	1493	<b>38.30</b>		0.5	$T = (3490.1 - H)/52.1$	52.1
Broken Gypsum Unit (base)	1420	<b>39.70</b>		0.5	$T = (3033.4 - H)/40.6$	40.6
Curled Gypsum Unit (top)	1103	<b>47.50</b>		0.8	$T = (2876.3 - H)/37.3$	37.3
Curled Gypsum Unit (base)	1047	<b>49.00</b>		0.8	$T = (3105 - H)/42$	42.0
Small Gypsum Unit (top)	837	<b>54.00</b>		0.5	$T = (1836 - H)/18.5$	18.5
Small Gypsum Unit (base)	800	<b>56.00</b>		0.5	$T = (5212.8 - H)/78.8$	78.8
Clastic breccia	725		56.95	0.7		78.8
<i>Lower Member</i>						
LGU (top)	603	<b>58.50</b>		1.0	$T = (2849.4 - H)/38.4$	38.4
LGU (base)	507	<b>61.00</b>		1.0	$T = (4141.2 - H)/59.6$	59.6
Clastic	247		65.36	1.0		59.6
Base of section	0	<b>69.51</b>		1.0		

*Comment:* Uncertainty reported at 68% confidence limit.

Table 7  
Summary of unified chronology ages for MSH section.

Stratigraphy	Height (cm)	Tuned anchor age (ka)	Regression age (ka)	Uncertainty (ka)	Regression age equation	Sedimentation rate (cm/ka)
<i>Middle Member</i>						
Broken Gypsum Unit (top)	1720	<b>38.30</b>		0.5	$T = (3361.4 - H)/42.9$	42.9
Broken Gypsum Unit (base)	1660	<b>39.70</b>		0.5	$T = (3889.3 - H)/56.2$	56.2
Curled Gypsum Unit (top)	1222	<b>47.50</b>		0.8	$T = (1918.7 - H)/14.7$	14.7
Curled Gypsum Unit (base)	1200	<b>49.00</b>		0.8	$T = (4757.4 - H)/72.6$	72.6
Convolute unit (top)	1080		50.65	0.7		72.6
Convolute unit (base)	1015		51.55	0.6		72.6
Small Gypsum Unit (top)	837	<b>54.00</b>		0.5	$T = (1836 - H)/18.5$	18.5
Small Gypsum Unit (base)	800	<b>56.00</b>		0.5	$T = (5862.4 - H)/90.4$	90.4
<i>Lower Member</i>						
LGU (top)	574	<b>58.50</b>		1.0	$T = (4107.4 - H)/60.4$	60.4
LGU (base)	423	<b>61.00</b>		1.0	$T = (3455.1 - H)/49.7$	49.7
Clastic	380		61.87	1.0		49.7
Clastic	350		62.47	1.0		49.7
Base of section	0	<b>69.51</b>		1.0		

*Comment:* Uncertainty reported at 68% confidence limit.

Table 8  
Summary of unified chronology ages for LP1 section.

Stratigraphy samples	Height (cm)	Tuned anchor age (ka)	Regression age (ka)	Uncertainty (ka)	Regression age equation	Sedimentation rate (cm/ka)
Upper Gypsum Unit (base)	2934	<b>17.10</b>		0.5	$T = (4050.3 - H)/65.3$	65.3
Broken Gypsum Unit (top)	1550	<b>38.30</b>		0.5	$T = (2831.7 - H)/33.5$	33.5
Clastic	1113		51.36	0.5		33.5
Hiatus (?)			?	?		
LGU (top)	874	<b>58.50</b>		1.0	$T = (5517.9 - H)/79.4$	79.4
Base of section	0	<b>69.51</b>		1.0		

*Comments:* Halite at ~11.13 m indicates a possible hiatus. This is supported by the preliminary regression ages which suggest significant decrease in sedimentation rates. Hence, the age–height model is not constrained between 8.74 and 11.13 m. Uncertainty reported at 68% confidence limit.

and MIS4. These shifts are not resolved in Bartov et al.'s (2003) lake level curve, but their ages, according to the Deir-Shaman age model (Table 5), are 42.42–41.57 ka for MMAU-I, and between 38.97 and 36.57 ka for MMAU II and III. These ages are in remarkable agreement with the tuned ages of *aad* bundles at PZ1 (Table 4), which imply corresponding age boundaries for MMAU-I, and MMAU-II and -III, of 43.07–41.08 ka and 38.30–36.23 ka, respectively.

#### 7.1.2. 'Delta age' and initial ( $^{234}\text{U}/^{238}\text{U}$ ) ratios

In order to strengthen the confidence in the age-model, we calculated the difference between the corrected single sample ages and the corresponding model (regression) age at each elevation point (henceforth, 'delta-age'). We then filtered out all single samples with a 'delta-age' larger than 3 ka. A common feature of the remaining samples is that they all display initial ( $^{234}\text{U}/^{238}\text{U}$ ) ratios within a significantly narrow range of  $1.521 \pm 0.030$  ( $1\sigma$ ) compared to the unfiltered data set displaying  $1.550 \pm 0.178$  (Fig. 12;

detritus samples are filtered out by considering only samples displaying initial ( $^{234}\text{U}/^{238}\text{U}$ ) ratios above 1.4).

This observation provides confidence in the validity of our filtering scheme and in the resulting age models. Moreover, the narrowing of the range of initial ( $^{234}\text{U}/^{238}\text{U}$ ) ratios implies that Lake Lisan maintained a well-defined characteristic ( $^{234}\text{U}/^{238}\text{U}$ ) composition and that samples deviating from it reflect admixing of detrital material of an unknown composition, or alternatively, diagenetic alteration. Hence, similar to the approach used in coral dating, samples deviating from an accepted ( $^{234}\text{U}/^{238}\text{U}$ ) "Lisan range" should be considered with caution, or rejected for the purpose of conventional U–Th dating. This approach can be used to evaluate the validity of lake sediment U–Th ages in other sites where no stratigraphic constraints are available.

Considering the individual sections, the average initial ( $^{234}\text{U}/^{238}\text{U}$ ) values for NT, BA, MSH, M1, LP1 and PZ1 are  $1.521 \pm 0.019$ ,  $1.531 \pm 0.089$ ,  $1.591 \pm 0.041$ ,  $1.525 \pm 0.032$ ,  $1.526 \pm 0.013$  and  $1.508 \pm 0.019$ , respectively. The

MSH section clearly deviates toward high values compared to the other sections, in concert with similar age offsets, most likely suggesting some impact of diagenetic alteration.

## 7.2. Lake levels

The integrated multi-site chronology of the Lisan Fm. allows us to re-examine the Lisan lake level curve reconstruction. The age-tuned columnar sections of PZ1, NT, and M1 are presented in Fig. 13 and compared to available lake level reconstructions for Lake Lisan and the Holocene Dead Sea. Of interest here are the studies of Bartov et al. (2003, 2006) and Lisker et al. (2009) (blue and red<sup>2</sup> curves in Fig. 13, respectively). The former reconstruction is based on ages and elevations of various lake level indicators found in sediment sections and paleo-shores throughout the DSB, while the latter is based on the presence of authigenic aragonite deposits in elevated caves overhanging the DSB.

Bartov et al.'s (2003, 2006) reconstruction implies the highest lake stand existed during MIS2 and to a lesser extent during MIS4, while MIS3 was characterized by moderate stands at ca. 270 m-bmsl that are punctuated by several abrupt lake level drops, although the data set used for this reconstruction is sparse for the MIS3 time window. Alternatively, the Lisker et al. (2009) curve implies high lake levels from ca. 48–45 ka until ~16–17 ka, with very little temporal variability. This reconstruction does not display any millennial-scale perturbations or correspondence to the lacustrine stratigraphic sections discussed here, where the Middle Member corresponding to MIS3 is characterized by frequent lithological changes between sequences of primary aragonite, gypsum and detritus, as well as the appearance of significant sedimentary hiatuses. Thus, the Lisker et al. (2009) curve can only be referred to in the context of a general upper-limit envelope. Our observations agree with the Bartov et al. (2003, 2006) curve though the full data set of lake level indicators, in particular those corresponding to MIS3, is re-evaluated according to the new chronology presented here in a separate publication (Torfstein et al., 2013).

## 8. SUMMARY

Despite their importance in reconstructing Quaternary climate changes in continental environments, lacustrine deposits present a major challenge for establishing precise and accurate chronologies. We have applied an iterative multi-site dating approach that provides a framework for the deconvolution of the chronology of sites in the DSB as well as in other lacustrine environments.

Our integrated multi-site chronology of Lake Lisan (~70–14 ka) is based on U–Th and complementary radiocarbon ages of primary aragonites from several sections along the Dead Sea basin and the Jordan Valley: the Massada (MI), Beit-Ha'arava (BA), Nahal Mishmar (MSH) and

Lisan Peninsula (LPI) sections at the central part of the basin, the Deir-Shaman (NT) section at the central Jordan Valley and the previously (Haase-Schramm et al., 2004) dated and documented PZ1 section at the Perazim Valley. The U–Th-based age models were established for each section by correcting for detrital U and Th, and hydrogenous Th present in the primary aragonite samples. A specific detrital end member (DEM) correction value was derived for each coeval set of aragonite samples. In general, the DEM composition in all the studied sites, covering more than 100 km of the length of Lake Lisan, overlaps and agrees with previous assessments.

The independent age models constructed for each individual Lisan Formation section show that within error, discrete events of massive gypsum deposition were synchronous with Heinrich events, when iceberg armadas discharged into the North Atlantic triggering abrupt climate changes on a global scale. We use this connection to fine-tune the age of the gypsum units in the Lisan Formation according to well-dated records in Chinese caves corresponding to H6 (61–58.5 ka), H5a (56–54 ka), H5 (49–47.5 ka), H4 (39.7–38.3 ka) and H1 (17.1–15.5 ka). A final iteration step involves the construction of a unified set of regression ages for each section. The age uncertainties limit typically range between 1000 and 2000 years (95% confidence limit) throughout 70–14 ka. These uncertainties are well below those typically related to individual U–Th and radiocarbon dates of “dirty” carbonates, demonstrating the advantage of the multi-site iterative age model construction. The initial (<sup>234</sup>U/<sup>238</sup>U) ratios of aragonite samples display an average value of  $1.550 \pm 0.178$  ( $1\sigma$ ), yet when considering only samples whose U–Th ages correspond to the unified age model, this value shifts and displays a significantly narrower range of  $1.521 \pm 0.030$ , suggesting that Lake Lisan was characterized by a constant (<sup>234</sup>U/<sup>238</sup>U) composition and that deviations from this composition imply detrital contamination or diagenetic alteration.

The M1, BA, MSH and LPI sections are characterized by sequences of alternating aragonite–detritus (aad), marking deep-lake depositional environments. In these sections, the aad intervals are interrupted by discrete gypsum units, which mark lake level drops. An increased resolution of abrupt climate perturbations during low or intermediate water stand stages is available at the marginal PZ1 and NT sections, which are characterized by marginal (clastic) sediment facies. There, repeated oscillations in lithology are identified particularly during MIS3, and are associated with the impact of Greenland stadial–interstadial cycles, though the nature of this connection remains unclear. Overall, Lake Lisan reflects a cold and wet climate regime that existed in the catchment throughout the last glacial cycle.

The iterative multi-site dating approach presented here provides a framework for the deconvolution of the chronology of other sites in the DSB as well as in other lacustrine environments.

## ACKNOWLEDGMENTS

The U–Th isotope analyses were conducted at the Geological Survey of Israel and benefited from the advice and assistance of

<sup>2</sup> For interpretation of color in Fig. 13, the reader is referred to the web version of this article.

Irina Segal, Nataliya Teplyakov, Olga Yoffe and Ludwig Halicz. We also thank Udi Coddington and Keren Sarusi for assistance in field and lab work. The comments and suggestions of three anonymous reviewers are appreciated and helped improve this manuscript considerably. Funding was provided by the Binational Science Foundation (BSF) Grant No. 2006.363 to M.S. and S.G.

#### APPENDIX A. SUPPLEMENTARY DATA

Supplementary data associated with this article can be found, in the online version, at <http://dx.doi.org/10.1016/j.gca.2012.11.003>.

#### REFERENCES

- Bar-Matthews M., Ayalon A., Gilmour A. and Hawkesworth C. J. (2003) Sea-land oxygen isotopic relationships from planktonic foraminifera and speleothems in the Eastern Mediterranean region and their implication for paleorainfall during interglacial intervals. *Geochim. Cosmoch. Acta* **67**, 3181–3199.
- Bartov Y. (1999) The geology of the Lisan Formation in the central Dead Sea basin. MSc thesis, the Hebrew University of Jerusalem.
- Bartov Y. (2004) Sedimentary fill analysis of a continental basin—the late Pleistocene Dead Sea. Ph.D. dissertation, Hebrew University of Jerusalem.
- Bartov Y., Stein M., Enzel Y., Agnon A. and Reches Z. (2002) Lake levels and sequence stratigraphy of Lake Lisan, the Late Pleistocene precursor of the Dead Sea. *Quat. Res.* **57**, 9–21.
- Bartov Y., Goldstein S. L., Stein M. and Enzel Y. (2003) Catastrophic arid episodes in the Eastern Mediterranean linked with the North Atlantic Heinrich events. *Geology* **31**, 439.
- Bartov Y., Agnon A., Enzel Y. and Stein M. (2006) Late Quaternary faulting and subsidence in the central Dead Sea basin. *Israel J. Earth Sci.* **55**, 17–31.
- Begin Z. B., Ehrlich A. and Nathan Y. (1974) Lake Lisan, the Pleistocene precursor of the Dead Sea. *Geol. Surv. Israel Bull.* **63**, 30.
- Bischoff J. L. and Fitzpatrick J. A. (1991) U-series dating of impure carbonates: an isochron technique using total-sample dissolution. *Geochim. Cosmochim. Acta* **55**, 543–554.
- Bookman (Ken-Tor) R., Enzel Y., Agnon A. and Stein M. (2004) Late Holocene lake levels of the Dead Sea. *Bull. Geol. Soc. Am.* **116**, 555–571.
- Bookman R., Bartov Y., Enzel Y. and Stein M. (2006) Quaternary lake levels in the Dead Sea basin: two centuries of research. *GSA Spec. Pap.* **401**, 155.
- Broecker W. (1963) A preliminary evaluation of uranium series inequilibrium as a tool of absolute age measurement on marine carbonates. *J. Geophys. Res.* **68**, 2817–2834.
- Bronk Ramsey C. (2009) Bayesian analysis of radiocarbon dates. *Radiocarbon* **51**, 337–360.
- Cheng H., Edwards R. L., Hoff J., Gallup C. D., Richards D. A. and Asmerom Y. (2000) The half-lives of uranium-234 and thorium-230. *Chem. Geol.* **169**, 17–33.
- Haase-Schramm A., Goldstein S. L. and Stein M. (2004) U–Th dating of Lake Lisan (late Pleistocene Dead Sea) aragonite and implications for glacial east Mediterranean climate change. *Geochim. Cosmochim. Acta* **68**, 985–1005.
- Hemming S. R. (2004) Heinrich events: Massive late Pleistocene detritus layers of the North Atlantic and their global climate imprint. *Rev. Geophys.* **42**, 1005.
- Israelson C., Björck S., Hawkesworth C. J. and Possnert G. (1997) Direct U–Th dating of organic- and carbonate-rich lake sediments from southern Scandinavia. *Earth Planet. Sci. Lett.* **153**, 251–263.
- Jaffey A. H., Flynn K. F., Glendenin L. E., Bentley W. C. and Essling A. M. (1971) Precision measurement of half-lives and specific activities of  $^{235}\text{U}$  and  $^{238}\text{U}$ . *Phys. Rev.* **4**, 1889–1907.
- Katz A., Kolodny Y. and Nissenbaum A. (1977) The geochemical evolution of the Pleistocene Lake Lisan-Dead Sea system. *Geochim. Cosmoch. Acta* **41**, 1609–1626.
- Kaufman A. (1971) U-series dating of Dead Sea basin carbonates. *Geochim. Cosmochim. Acta* **35**, 1269–1281.
- Kaufman A. (1993) An evaluation of several methods for determining ages in impure carbonates. *Geochim. Cosmochim. Acta* **57**, 2303–2317.
- Kaufman A., Yechieli Y. and Gardosh M. (1992) Reevaluation of the lake-sediment chronology in the Dead Sea basin, Israel, based on new  $^{230}\text{Th}/\text{U}$  dates. *Quatern. Res.* **38**, 292–304.
- Ku T.-L., Luo S., Lowenstein T. K., Li J. and Spencer R. J. (1998) U-series chronology of lacustrine deposits in Death Valley, California. *Quatern. Res.* **50**, 261–275.
- Ku T. L. and Liang Z. C. (1984) The dating of impure carbonates with decay-series isotopes. *Nucl. Instrum. Methods Phys. Res.* **223**, 563–571.
- Le Roux L. J. and Glendenin L. E. (1963) Half-life of  $^{232}\text{Th}$ . In *Proceedings of the National Meeting on Nuclear Energy*, Pretoria, South Africa.
- Lin J. C., Broecker W. S., Anderson R. F., Hemming S., Rubenstone J. L. and Bonani G. (1996) New  $^{230}\text{Th}/\text{U}$  and  $^{14}\text{C}$  ages from Lake Lahontan carbonates, Nevada, USA, and a discussion of the origin of initial thorium. *Geochim. Cosmochim. Acta* **60**, 2817–2832.
- Lisker S., Vaks A., Bar-Matthews M., Porat N. and Frumkin A. (2009) Stromatolites in caves of the Dead Sea Fault Escarpment: implications to latest Pleistocene lake levels and tectonic subsidence. *Quat. Sci. Rev.* **28**, 80–92.
- Ludwig K. R. (2003) Mathematical–statistical treatment of data and errors for  $^{230}\text{Th}/\text{U}$  geochronology. *Rev. Mineral. Geochem.* **52**, 631.
- Ludwig K. R. and Titterton D. M. (1994) Calculation of isochrons, ages, and errors. *Geochim. Cosmochim. Acta* **58**, 5031–5042.
- Luo S. and Ku T.-L. (1991) U-series isochron dating: a generalized method employing total-sample dissolution. *Geochim. Cosmochim. Acta* **55**, 555–564.
- Machlus M., Enzel Y., Goldstein S. L., Marco S. and Stein M. (2000) Reconstructing low levels of Lake Lisan by correlating fan-delta and lacustrine deposits. *Quatern. Int.* **73–74**, 137–144.
- Marco S. (1996) Paleomagnetism and Paleoseismology in the Late Pleistocene Dead Sea Graben. Ph.D. dissertation, Hebrew University of Jerusalem.
- Migowski C., Stein M., Prasad S., Negendank J. F. W. and Agnon A. (2006) Holocene climate variability and cultural evolution in the Near East from the Dead Sea sedimentary record. *Quatern. Res.* **66**, 421–431.
- Neuv D. and Emery K. D. (1967) The Dead Sea, depositional processes and environments of evaporites. *Geol. Surv. Israel Bull.* **41**, 147.
- Partin J. W., Cobb K. M., Adkins J. F., Clark B. and Fernandez D. P. (2007) Millennial-scale trends in west Pacific warm pool hydrology since the Last Glacial Maximum. *Nature* **449**, 452–455.
- Prasad S., Vos H., Negendank J. F. W., Waldmann N., Goldstein S. L. and Stein M. (2004) Evidence from Lake Lisan of solar influence on decadal- to centennial-scale climate variability during marine oxygen isotope stage 2. *Geology* **32**, 581.
- Richards D. A. and Dorale J. A. (2003) Uranium-series chronology and environmental applications of speleothems. *Rev. Mineral. Geochem.* **52**, 407–460.

- Schramm A., Stein M. and Goldstein S. L. (2000) Calibration of the  $^{14}\text{C}$  time scale to  $>40$  ka by  $^{234}\text{U}$ – $^{230}\text{Th}$  dating of Lake Lisan sediments (last glacial Dead Sea). *Earth Planet. Sci. Lett.* **175**, 27–40.
- Stein M. (2001) The sedimentary and geochemical record of Neogene–Quaternary water bodies in the Dead Sea Basin— inferences for the regional paleoclimatic history. *J. Paleolimnol.* **26**, 271–282.
- Stein M. and Goldstein S. L. (2006) U–Th and radiocarbon chronologies of late Quaternary lacustrine records of the Dead Sea basin: methods and applications. *GSA Spec. Pap.* **401**, 141–154.
- Stein M., Starinsky A., Katz A., Goldstein S. L., Machlus M. and Schramm A. (1997) Strontium isotopic, chemical, and sedimentological evidence for the evolution of Lake Lisan and the Dead Sea. *Geochim. Cosmochim. Acta* **61**, 3975–3992.
- Stein M., Torfstein A., Gavrieli I. and Yechieli Y. (2010) Abrupt aridities and salt deposition in the post-glacial Dead Sea and their North Atlantic connection. *Quat. Sci. Rev.* **29**, 567–575.
- Torfstein A., Goldstein S. L., Stein M. and Enzel Y. (2013) Impacts of abrupt climate changes in the Levant from last glacial Dead Sea levels. *Quatern. Sci. Rev.* submitted for publication.
- Torfstein A., Gavrieli I., Katz A., Kolodny Y. and Stein M. (2008) Gypsum as a monitor of the paleo-limnological–hydrological conditions in Lake Lisan and the Dead Sea. *Geochim. Cosmochim. Acta* **72**, 2491–2509.
- Torfstein A., Gavrieli I. and Stein M. (2005) The sources and evolution of sulfur in the hypersaline Lake Lisan (paleo-Dead Sea). *Earth Planet. Sci. Lett.* **236**, 61–77.
- Torfstein A., Haase-Schramm A., Waldmann N., Kolodny Y. and Stein M. (2009) U-series and oxygen isotope chronology of the mid-Pleistocene Lake Amora (Dead Sea basin). *Geochim. Cosmochim. Acta* **73**, 2603–2630.
- Waldmann N., Starinsky A. and Stein M. (2007) Primary carbonates and Ca-chloride brines as monitors of a paleo-hydrological regime in the Dead Sea basin. *Quatern. Sci. Rev.* **26**, 2219–2228.
- Waldmann N., Stein M., Ariztegui D. and Starinsky A. (2009) Stratigraphy, depositional environments and level reconstruction of the last interglacial Lake Samra in the Dead Sea basin. *Quatern. Res.* **72**, 1–15.
- Wang Y., Cheng H., Edwards R. L., Kong X., Shao X., Chen S., Wu J., Jiang X., Wang X. and An Z. (2008) Millennial- and orbital-scale changes in the East Asian monsoon over the past 224,000 years. *Nature* **451**, 1090–1093.
- Wang Y. J., Cheng H., Edwards R. L., An Z. S., Wu J. Y., Shen C.-C. and Dorale J. A. (2001) A high-resolution absolute-dated late Pleistocene monsoon record from Hulu Cave, China. *Science* **294**, 2345–2348.
- Wendt I. and Carl C. (1991) The statistical distribution of the mean squared weighted deviation. *Chem. Geol.* **86**, 275–285.
- Wolff E. W., Chappellaz J., Blunier T., Rasmussen S. O. and Svensson A. (2010) Millennial-scale variability during the last glacial: the ice core record. *Quatern. Sci. Rev.* **29**, 2828–2838.
- Yechieli Y., Magaritz M., Levy Y., Weber U., Kafri U., Woelfli W. and Bonani G. (1993) Late Quaternary geological history of the Dead Sea area, Israel. *Quatern. Res.* **39**, 59–67.

Associate editor: Yuri Amelin